



Diurnal coastal trapped waves propagating along the east coast of the Shimokita Peninsula, Japan

Teiji In¹ · Tomoyuki Kuji¹ · Hisaki Kofuji¹ · Tomoharu Nakayama¹

Received: 24 March 2023 / Revised: 17 June 2023 / Accepted: 18 August 2023 / Published online: 1 September 2023
© The Author(s) 2023

Abstract

In this study, we investigated diurnal coastal trapped waves in the eastern coastal area of the Shimokita Peninsula near the Tsugaru Strait. The coastal trapped waves in this area have not yet been observed. We observed current velocities at three sites on the coast to clarify the propagation and seasonal features. We also used an ocean general circulation model to determine the detailed structure and the causes underlying the seasonal characteristics of the waves. The coastal trapped waves propagated southward along the coast from the strait, where significant tidal currents exist. Coastal trapped waves depend on cross-shelf length and stratification strength. The coastal trapped waves propagate as internal Kelvin waves from summer to early winter in the northern part of the peninsula (where the shelf is narrow) and as shelf waves in the southern part (where the shelf is wide). From late winter to spring, the coastal trapped waves practically disappear in the northern part of the peninsula owing to the vertical uniform density off the east coast and the small cross-shelf width in the northern part. In autumn, the tidal current flows north of the sill near Cape Shiriya at the eastern mouth of the straits owing to the northward shift of the Tsugaru Warm Current in the strait; thus, the coastal trapped waves along the Shimokita coast weaken.

Keywords Coastal trapped wave · Tsugaru strait · Tsugaru Warm Current · Tide

1 Introduction

Shimokita Peninsula is located in northernmost Honshu Island, Japan, bordering the Tsugaru Strait to the north, Mutsu Bay to the west, and the North Pacific Ocean to the east (Fig. 1). The Tsugaru Warm Current (TWC) flows from the Sea of Japan to the North Pacific Ocean through the Tsugaru Strait. As the TWC is a branch of the Tsushima Warm Current, which flows into the Japan Sea via the Tsushima Strait (Isobe 1999), the water mass in the TWC has features of the North Pacific subtropical zone, characterized by higher temperatures and salinity relative to those of the Oyashio water. The volume of water transported in the TWC is estimated to be 1.4 Sv ($1 \text{ Sv} = 1 \times 10^6 \text{ m}^3 \text{ s}^{-1}$) on average, based on previous observations (Shikama 1994; Onishi and Ohtani 1997; Ito et al. 2003). Although the variation is smaller than that in the Tsushima and Soya Warm Currents (Onishi and Ohtani 1997), the TWC has characteristic

seasonal variations in the North Pacific Ocean—east of the Tsugaru Strait—and Hidaka Bay (Conlon 1982), which considerably influence the velocity field and stratification on the Pacific side of Shimokita Peninsula. High-frequency ocean radar (HF radar) observations of the Tsugaru Strait have recently revealed seasonal variations in the flow axis of the TWC within the Tsugaru Strait (Yasui et al. 2022).

Tidal currents also contribute significantly to the flow structure in the Tsugaru Strait, as revealed using velocity observations from acoustic Doppler current profilers (ADCPs; Onishi et al. 2004; Kuroda et al. 2004). Luu et al. (2011) successfully reproduced barotropic tides in the Tsugaru Strait using a barotropic tidal model with realistic geometry and topography. They showed that residual tidal currents occur offshore of capes Tappi, Oma, and Shiriya; the vorticity arising at the headlands and adjacent sills is essential for the formation of residual currents. As little observational knowledge exists regarding current velocities on the east coast of the Shimokita Peninsula, the influence of strong tides in the Tsugaru Straits on the east coast of the Shimokita Peninsula remains unclear. As for the Soya Strait, diurnal tides have been observed propagating south-eastward from the strait to the coast of the Sea of Okhotsk

✉ Teiji In
in@jmsfmml.or.jp

¹ Japan Marine Science Foundation, Mutsu, Aomori, Japan

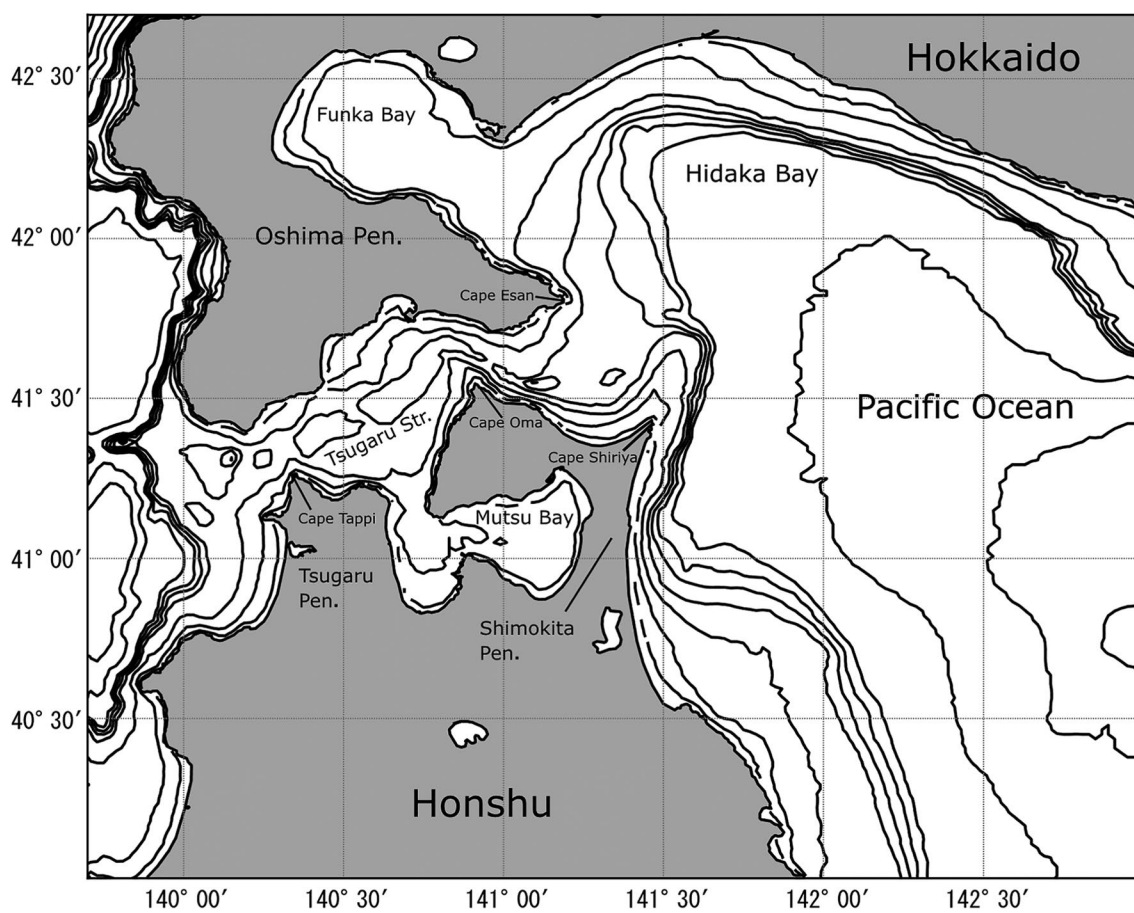


Fig. 1 Geometry and topography around the Shimokita Peninsula. The bottom depth contour lines are at 20, 50, 100, 200, 300, 400, 500, 1000, 1500, 2000, 2500, 3000, 3500, and 4000 m

in Hokkaido (Odamaki 1994). Homma et al. (2017) performed numerical experiments using a three-dimensional (3-D) nonhydrostatic model to investigate the internal waves in the Tsugaru Strait. They inferred the existence of daily period coastal trapped waves (CTWs) propagating southward from the Tsugaru Strait along the east coast of the Shimokita Peninsula and northward along the west coast of the Oshima Peninsula; however, the details of these waves remain unclear.

Theoretical and modeling studies conducted in the 1970s and 1980s revealed the mechanism of CTWs (Wang and Mooers 1976; Huthnance 1978; Brink 1982), which are waves trapped on a coastal continental shelf that propagate along the right-hand side of a shore in the Northern Hemisphere. Internal gravity due to stratification and topographic beta effects provide a restoring force for CTWs. When the land is vertically sheared, relative vorticity is not generated because of the slope; therefore, the wave behaves like classic baroclinic coastal Kelvin waves. In contrast, if the density in the vertical direction is constant, the waves behave like barotropic continental shelf waves. The cross-shelf width along

the east coast of Shimokita Peninsula changes significantly at approximately 41° N, with a steep slope on the north side and a gentle slope on the south side (Fig. 1), implying that the shape of CTWs differs between the north and south. The seasonal stratification variation in this area depends on the seasonal relative density of the TWC and Oyashio Current and is subject to the seasonal form change in the TWC (Conlon 1982).

As mentioned above, the Tsugaru Strait is subject to significant variability on various time scales. However, the impact of these variations on the variability in the eastern Tsugaru Strait is not fully understood. In particular, the influence of significant tidal flow variations within the Tsugaru Strait on the area is not clearly understood. Diurnal tides are expected to behave like CTWs because they are subinertial (Huthnance 1978). In this study, we investigated the CTWs on the east coast of the Shimokita Peninsula, which had been suggested to exist by a model simulation (Homma et al. 2017) but have not been observed, using observations around the Shimokita coastal area and an ocean general circulation model, incorporating tides. The behavior of the

CTWs at each location and season was analyzed by focusing on the shelf shape and seasonal stratification variations that substantially impact them. This study enhances our understanding of the strong short-term variability in the coastal area of the Shimokita Peninsula. It is expected to significantly contribute to the prediction of radionuclide migration in this area from nuclear facilities and fisheries using fixed nets.

2 Observations

Velocity observations were collected at three sites—A, B, and C (Fig. 2a). At sites A and B, the velocity was measured using electromagnetic current meters (INFINITY-EM by the JFE Advantech) from August 28 to November 29, 2011 (Period 1) and from May 10 to September 10, 2013 (Period 2). The depth of the current meter was 5.5 m in Period 1 and 10 m in Period 2 at sites A and B. At site C, velocity measurements since 2003, from a depth of approximately 10 m, were obtained from the ADCP attached to a mooring placed in 2002. The bottom depths

at sites A and B were approximately 20 m, and site C had a depth of approximately 40 m. The linear distances between sites A and B and sites B and C were 23.0 and 8.9 km, respectively. The time interval of the data is 10 min at sites A and B and 5 min at site C.

Conlon (1982) observed that the TWC forms a clockwise gyre off the east coast of the Shimokita Peninsula and in the Hidaka Bay area during the warm season (gyre mode) and flows southward along the east coast of the Shimokita Peninsula during the cold season (coastal mode). To investigate the water mass structure associated with this seasonality, we collected observations with expendable conductivity, temperature, and depth profiling systems (XCTD) at nine stations, St.1–9, along the ferry course (Fig. 2b). Table 1 shows the observation periods from 2011 to 2013, including the transition periods of the TWC from coastal to gyre mode and vice versa.

The observation data used to validate the model's barotropic tides are astronomical tidal data from the tidal gauges in Table 2 from 2011 to 2013. These data are available from the Japan Meteorological Agency (JMA) website.

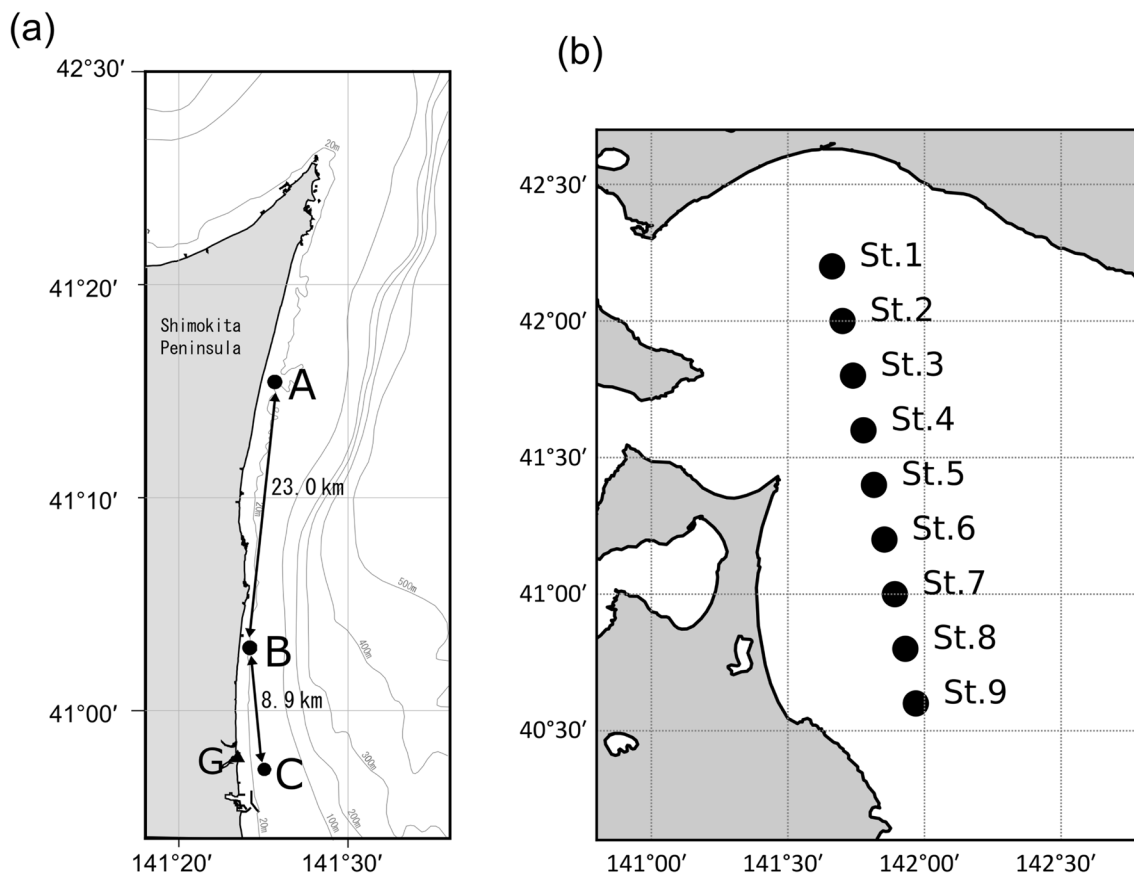


Fig. 2 **a** Velocity observation sites. The velocity was observed using electromagnetic current meters in sites A and B and using ADCP in site C. The linear distances between sites A and B and sites B and C

were 23.0 and 8.9 km, respectively. Point G represents the location of the Mutsu-Ogawara tidal gauge. **b** XCTD observation stations on the ferry ship course

Table 1 Dates of the XCTD observations on the ferry ship course

Year	Month, day					
2011	May, 9	May, 25	Jun, 22	Jul, 14	Aug, 3	Sep, 8
	Oct, 6	Nov, 1	Dec, 1			
2012	Jan, 10	Feb, 14	Mar, 1	Apr, 20	May, 18	Jun, 7
	Jul, 3	Aug, 2	Sep, 7	Oct, 5	Nov, 2	Dec, 4
2013	Jan, 9	Feb, 8	Mar, 6	Apr, 19	Jun, 4	
	Jul, 2	Aug, 1	Oct, 1	Nov, 7	Dec, 17	

Table 2 Locations of the tidal gauges

Tidal gauge	Latitude	Longitude	Tidal gauge	Latitude	Longitude
Ishikari-Shinko	43° 13'	141° 18'	Okushiri-Ko	42° 10'	139° 31'
Iwanai	42° 59'	140° 30'	Esashi	41° 52'	140° 8'
Suttsu	42° 48'	140° 14'	Aomori	40° 50'	140° 46'
Otaru	43° 12'	141° 0'	Asamushi	40° 54'	140° 52'
Nemuro	43° 21'	145° 35'	Hachinohe	40° 32'	141° 32'
Hanasaki	43° 17'	145° 34'	Shimokita	41° 22'	141° 14'
Kiritappu	43° 5'	145° 7'	Fukaura	40° 39'	139° 56'
Kushiro	42° 59'	144° 22'	Tappi	41° 15'	140° 23'
Tokachi	42° 18'	143° 19'	Oma	41° 32'	140° 54'
Tomakomai-Higashi	42° 36'	141° 49'	Ominato	41° 15'	141° 9'
Tomakomai-Nishi	42° 38'	141° 37'	Mutsu-Ogawara	40° 56'	141° 23'
Muroran	42° 21'	140° 57'	Oga	39° 57'	139° 42'
Shiraoi	42° 31'	141° 19'	Funakawa-Ko	39° 55'	139° 51'
Urakawa	42° 10'	142° 46'	Akita	39° 45'	140° 4'
Mori	42° 7'	140° 36'	Miyako	39° 39'	141° 58'
Yoshioka	41° 27'	140° 14'	Ofunato	39° 1'	141° 45'
Matsumae	41° 25'	140° 4'	Kamaishi	39° 16'	141° 53'
Hakodate	41° 47'	140° 43'	Kuji	40° 12'	141° 48'
Setana	42° 27'	139° 51'	Tobishima	39° 11'	139° 33'
Okushiri	42° 5'	139° 29'	Sakata	38° 55'	139° 49'

3 Model

3.1 Model description

The model used in this study was the Meteorological Research Institute Common Model (MRI.COM) developed by the Meteorological Research Institute of the Japan Meteorological Agency (JMA/MRI). This model adopts a spherical coordinate system, hydrostatic pressure approximation, Boussinesq approximation, and free surface. The model domain includes a part of the North Pacific Ocean, part of the Sea of Japan, and the Tsugaru Strait and reproduces the TWC and tidal currents. The horizontal model resolutions were $1/50^\circ$ and $1/70^\circ$ in the longitudinal and latitudinal directions, respectively, corresponding to approximately 1.5 km in both directions. The model domain was 139° – 147° E and $38^\circ 30'$ to $43^\circ 36'$ N. The lateral open boundary conditions for nesting were obtained

from the Four-dimensional Variational Ocean Reanalysis for the Western North Pacific (FORA-WMP30) developed by the Japan Agency for Marine–Earth Science and Technology and the JMA/MRI (Usui et al. 2017). The atmospheric conditions for the bulk sea surface heat and salt flux calculations were obtained from the National Centers of Environmental Prediction–Department of Energy atmospheric model (NCEP/DOE Reanalysis 2; Kanamitsu et al. 2002), and the wind speeds for wind stress calculations were obtained from the Grid Point Values of the Meso-Scale Model (GPV-MSM; Saito et al. 2006) developed by the JMA. The sea surface mixed layer model was developed by Noh and Kim (1999); the horizontal diffusions of potential temperature and salinity are isopycnal mixing (Gent and McWilliams 1990), and the horizontal viscosity of baroclinic velocity is biharmonic Smagorinsky viscosity (Griffies and Hallberg 2000). Internal tidal forcing was applied to the model, and the NAO.99b barotropic tidal values, developed by the National Astronomical

Observatory of Japan (Matsumoto et al. 2000), were added to the lateral open boundary conditions to reproduce the tides. The model was run from 2011 to 2013 and included velocity observations in the Shimokita coastal zone. The output intervals were recorded every hour.

3.2 Verification of barotropic tides

Figure 3 shows a comparison of the phase and amplitude of the four major tidal components in the harmonic analysis of the astronomical tide data. This was taken from 40 tide gauges included in the model domain and sea surface height to verify the reproducibility of the barotropic tides (Table 2). The model slightly underestimated the amplitude compared with the observations and accurately reproduced the phase. We used Eq. (1) (Hatayama et al. 1996; Luu et al. 2011) to quantitatively evaluate the error.

$$\text{RMS} = \frac{1}{N} \sum_{n=1}^N \left\{ \int_0^T \left[A_n^M \cos\left(\frac{2\pi}{T}t + \phi_n^M\right) - A_n^O \cos\left(\frac{2\pi}{T}t + \phi_n^O\right) \right]^2 dt \right\}^{1/2}, \quad (1)$$

where A and ϕ are the amplitude and period per tide station, respectively; the superscripts M and O represent the model and observation, respectively; T is the period; N is the total number of tide stations. The root-mean-square (RMS) errors at K1, O1, M2, and S2 were 1.39×10^{-2} , 1.40×10^{-2} , 1.28×10^{-2} , and 1.27×10^{-2} m, respectively. Compared to those reported by Luu et al. (2011), who used a barotropic tide model with a similar resolution targeting the same ocean domain, the errors were slightly smaller for all four major tidal components. Thus, the tidal level error was small, and the model reproducibility of the barotropic tides was adequate.

3.3 Verification of temperature and salinity

We tested the reproducibility of the water mass structure east of Shimokita Peninsula using the XCTD observations collected over the ferry course described in Sect. 2. The course crosses the gyre of the TWC during warm seasons; thus, these observations are suitable for understanding the transition between the gyre and coastal modes of the TWC. The reader can see the vertical distribution of XCTD observations and model values during Periods 1 and 2 of the velocity observation at sites A and B in Appendix A.

Figure 4 shows the RMS errors of temperature and salinity for the observations from 2011 to 2013 compared with those of the model. The RMS error for temperature decreased from spring to autumn and then increased throughout autumn, suggesting that both high temperatures and the differences in the position and size of the gyre caused larger errors (Appendix A). Salinity tended to be higher in spring, and this trend appeared to correspond to

the low-salinity water present in the surface layer in spring, which was small in the model. The average RMS errors over this period were 2.48 °C and 0.264 for water, temperature, and salinity, respectively.

The results presented in this section show that the model reproduces the water mass structure in the waters east of Shimokita Peninsula, although there were differences in the location of the gyre and the timing of its development from the observations. Therefore, it is possible to employ the model by considering the differences in the observations.

4 Analytical methods

In the previous section, we tested the reproducibility of barotropic tides using harmonic analysis for tidal levels. For the flow velocity, it is difficult to apply harmonic analysis owing to the significant seasonal variation in amplitude, as mentioned in the next section. To extract the diurnal variation, we applied band-pass filtering for the observational and modeled results using an FFT filter with a 23–27-h window, including the principal diurnal tidal constituents (Table 3).

To examine the propagation of the diurnal variation, we used the observed and modeled meridional velocities at sites A, B, and C in Fig. 2a. We determined the propagation velocity using the peak-to-peak and trough-to-trough time differences and the linear distances between sites A and B (23.0 km) and B and C (8.9 km). We obtained the maximum and minimum in the diurnal variation extracted by the band-pass filter above to determine the peak and trough of each site.

CTWs are the internal Kelvin waves if the shore vertically reaches the deep-sea floor. The phase speed of the internal Kelvin wave is the same as that of the internal gravity wave. It can be obtained for each mode by solving the Sturm–Liouville eigenvalue problem from the vertical density profile (e.g., Gill 1982). This method assumes a flat bottom and no current velocity. In the northern part of the Shimokita Peninsula coast, the cross-shelf width is small, the slope is steep, and the bottom below the shelf slope is gradual (Fig. 1). The current is gentle except to the east of the Tsugaru Strait, where the TWC flows out. These suggest that this method is most appropriate for the northern part of the Shimokita Peninsula coast. In the southern part of the Shimokita Peninsula coast, the influence of topography cannot be ignored due to the cross-shelf width expanding toward the south (Fig. 1). Huthnance (1978) showed that CTWs depend on the relative magnitudes of the internal gravity and cross-shelf width. The Burgers number, S , representing the relationship between the two, was estimated using Eq. (2).

Fig. 3 Scatter plots of the main four components with the harmonic analysis of the tide gauges and the model. From top to bottom, K1 (a, b), O1 (c, d), S2 (e, f), and M2 (g, h); the left column represents the amplitude, and the right column represents the phase

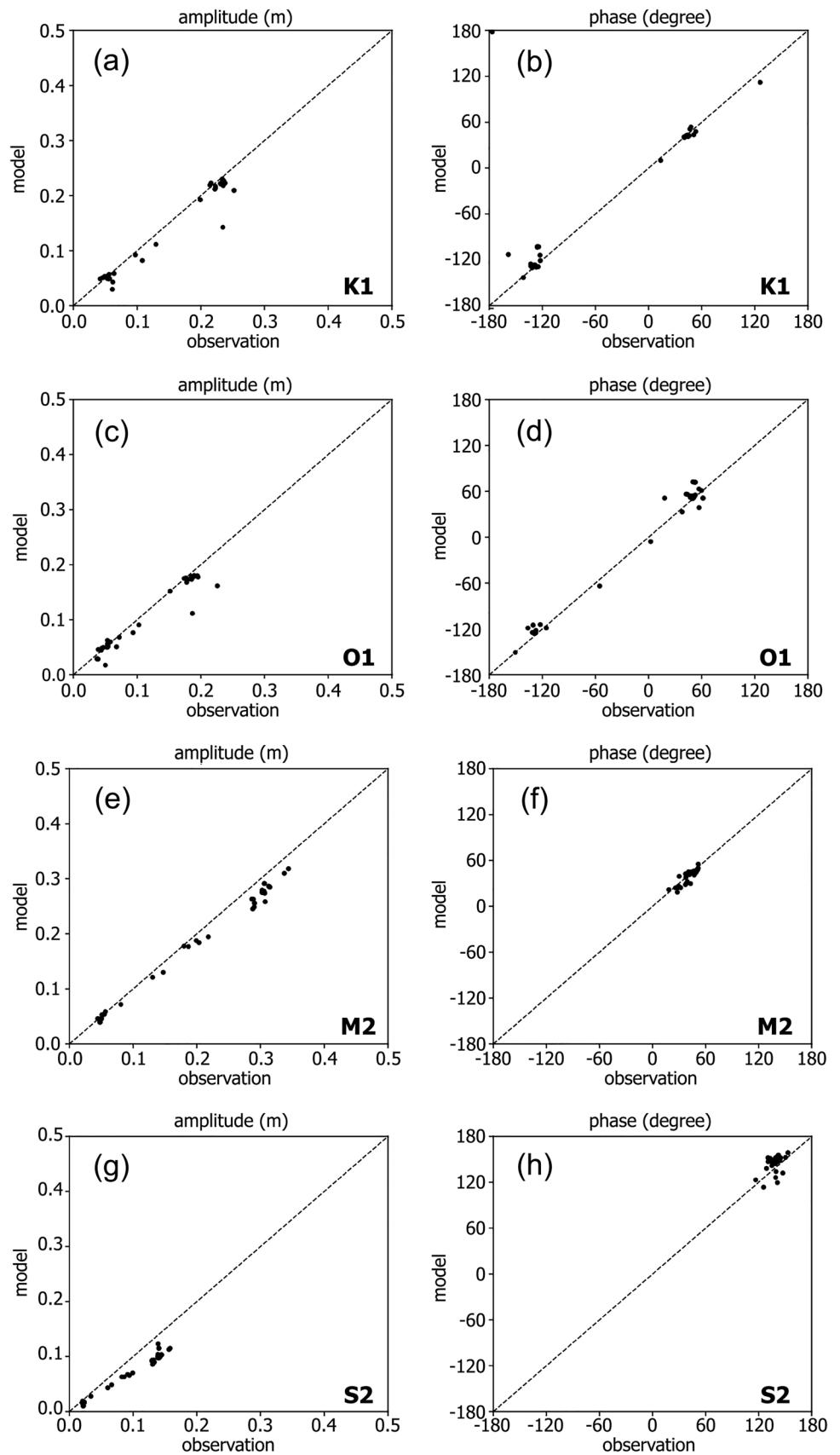


Fig. 4 Time series of observed and modeled mean-square errors for water temperature (a) and salinity (b)

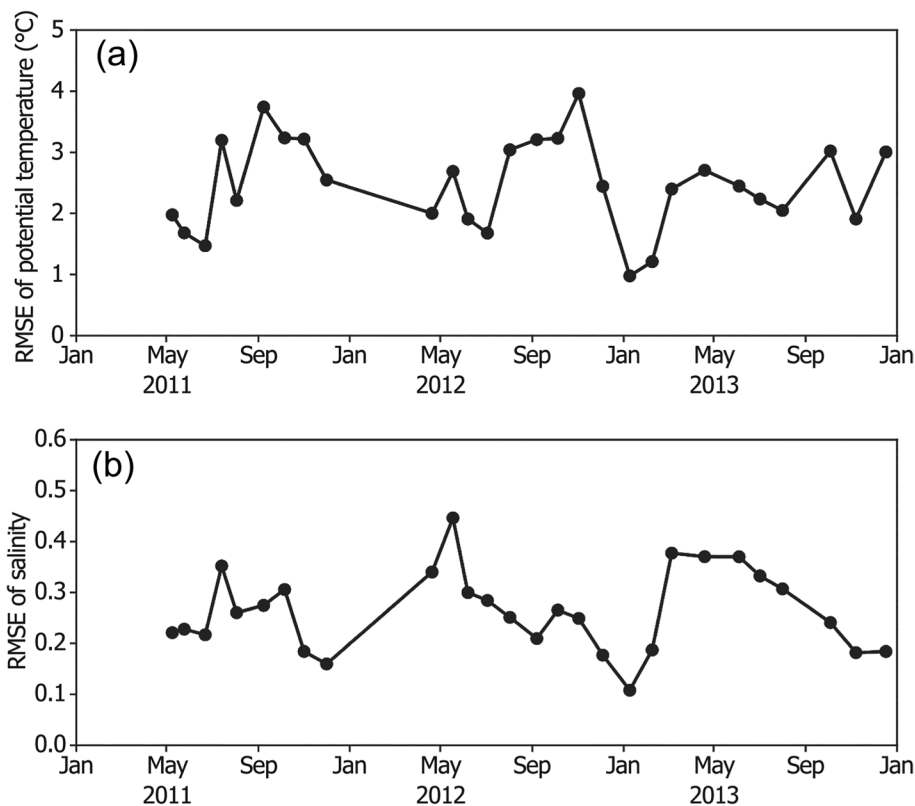


Table 3 Principal tidal constituents with semidiurnal and diurnal periods

Name	Period (h)
K2	11.97
S2	12.00
M2	12.42
N2	12.66
K1	23.93
P1	24.07
O1	25.82
Q1	26.87

the topographic beta effect. Expressing the Burgers number using the above vertical-mode decomposition, the Burgers number S_n for the n -th vertical mode is shown in Eq. (3).

$$S_n = \left(\frac{c_n}{fL} \right)^2 = \left(\frac{\lambda_{Dn}}{L} \right)^2, \tag{3}$$

where c_n and λ_{Dn} are the phase velocity and internal deformation radius of the internal gravity wave in the n -th mode, respectively.

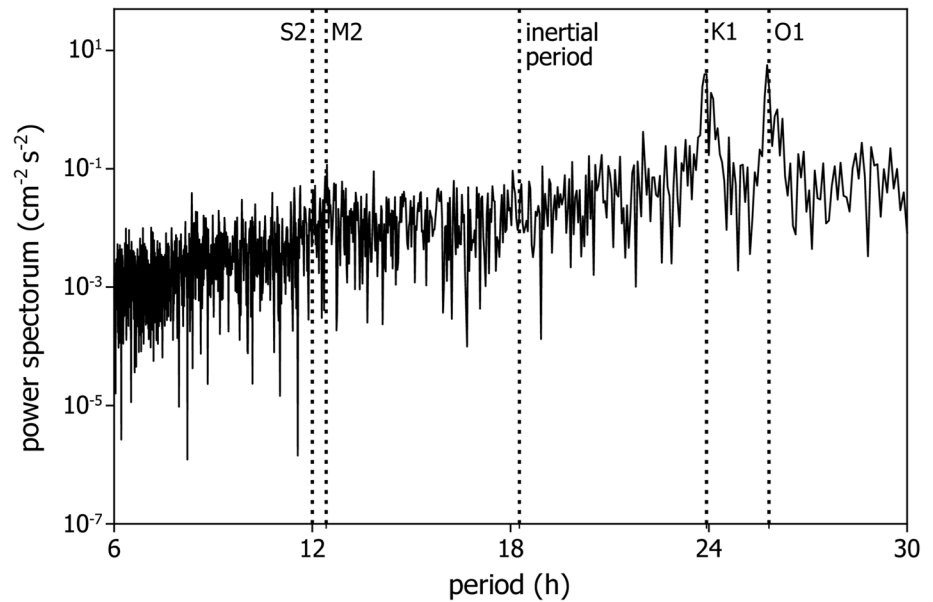
$$S = \left(\frac{N_0 H}{fL} \right)^2 = \left(\frac{\lambda_D}{L} \right)^2, \tag{2}$$

where N_0 , H , and L are the buoyancy frequencies, depths, and representative horizontal scales in the direction across the continental shelf, respectively; λ_D is the Rossby internal deformation radius; f is the Coriolis parameter. S is also the ratio of the Rossby internal deformation radius λ_D to L . S is sufficiently small when it is near-barotropic ($N_0 \sim 0$) or if the width of the shelf is large relative to the stratification. In this case, the contribution of the topographic beta effect was more significant than that of stratification, and the CTWs behaved as shelf waves. In the case of S being large, stratification was more significant than the contribution of

5 Diurnal variation and its propagation from the velocity observations

The velocity observation at site C (Fig. 2a) revealed that the predominant diurnal and weak semidiurnal velocities characterize the flow field in this region. Figure 5 shows the power spectrum of the meridional velocity at 10 m depth from the ADCP at site C for 2011, indicating that the diurnal period is dominated by tides, with sharply peaked maxima in the K1 and O1 tide periods. In contrast, the semidiurnal M2 and S2 tides were significantly smaller, without distinct peaks in each period. This result significantly differed from that of the tidal gauges. The amplitudes of the four major tidal components of the Mutsu-Ogawara tidal gauge (Table 2 and point G in Fig. 2a) near site C were 18.2, 22.3,

Fig. 5 Power spectrum obtained using the 10 m depth meridional velocity of the ADCP at site C. The period is one year, recorded in 2011

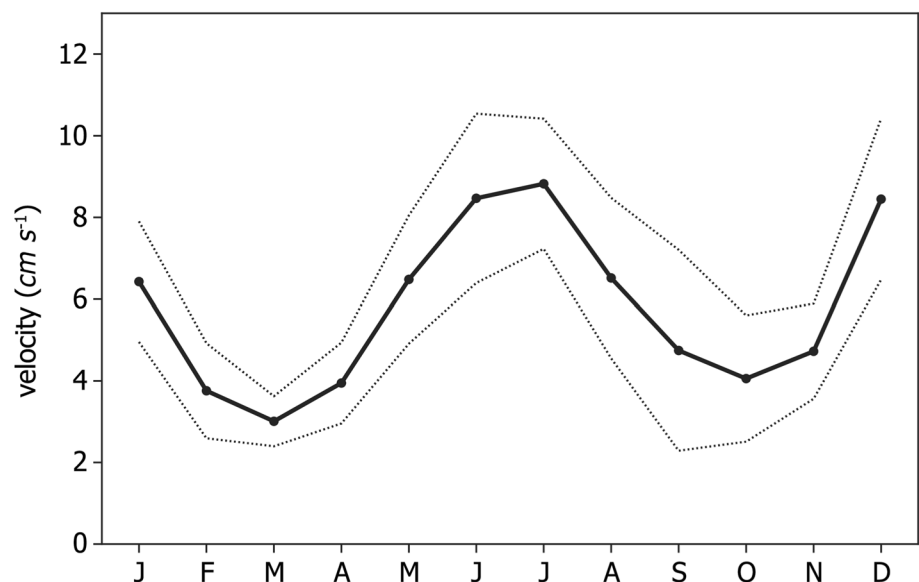


30.4, and 13.7 cm for O1, K1, M2, and S2, respectively. The magnitudes of the diurnal and semidiurnal cycle variations were comparable. These results suggest that baroclinic tides, rather than barotropic tides, dominate the tidal currents.

The long-term ADCP observations at site C indicated that the magnitude of diurnal variability in this area varies seasonally. Figure 6 shows the monthly mean magnitude of the diurnal variation, defined as band-pass filtered values in a 23–27-h window for the meridional velocity from 2004 to 2015. The magnitude of the diurnal variation had maxima in July and December and minima in March and October. The standard deviation was low in spring, increased through summer and autumn, and decreased in winter.

Next, we examined the propagation velocity of the diurnal variations using the three observation sites (sites A, B, and C in Fig. 2a). Figure 7 shows Hofmeyr diagrams of time and latitude for the hourly averaged meridional velocities observed at sites A, B, and C. The periods are May 12–14, 2013, for spring, July 5–7, 2013, for summer, and September 15–17, 2011, for autumn. On May 13, the propagation time from site A to site C was approximately 11 h. Using these time differences and the 32 km linear distance between sites A and C, the propagation velocity was approximately $70 \text{ cm} \cdot \text{s}^{-1}$. In July, the amplitude was larger, and the propagation speed was higher than those in May. The propagation time and speed from sites A to C were approximately 9 h and $100 \text{ cm} \cdot \text{s}^{-1}$. The diurnal velocity magnitude was the lowest

Fig. 6 Climatological monthly mean (solid line) of the magnitude of the flow velocity at site C for the diurnal variability from 2004 to 2015; the two dotted lines above and below the solid line represent the 1σ (standard deviation) and -1σ widths, respectively



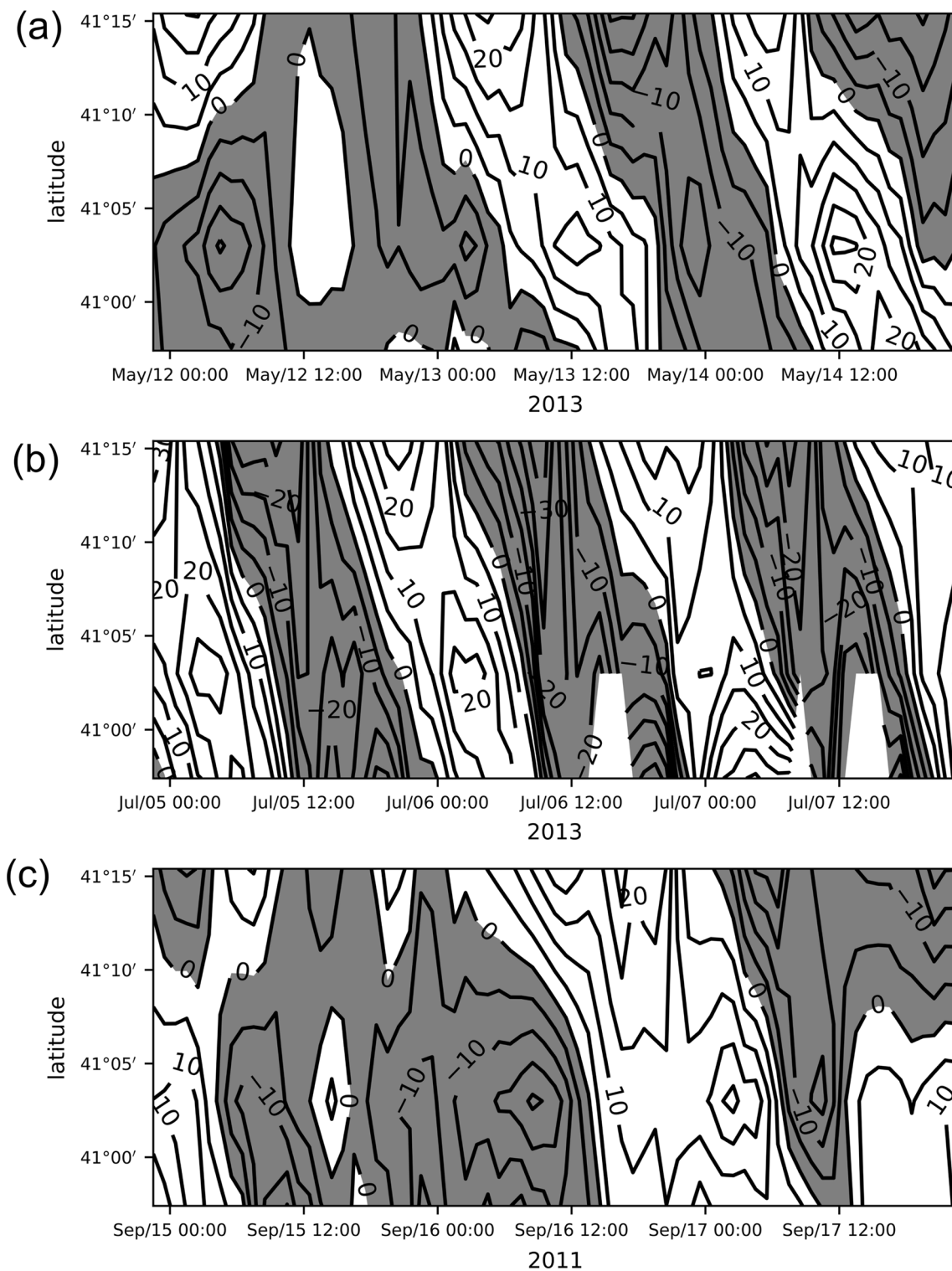
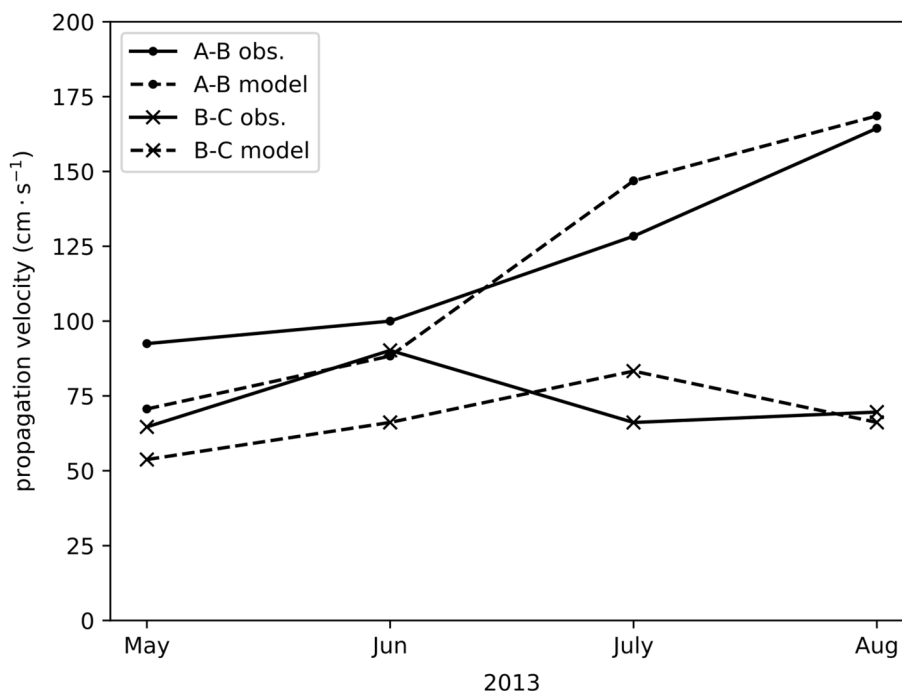


Fig. 7 Hofmeyr plots of observed meridional velocities versus latitude and time. The period is three days, May 12–14, 2013 (a), July 5–7, 2013 (b), and September 15–17, 2011 (c). The values are subtracted from the time-averaged value every three days. Negative values are shaded.

Fig. 8 Monthly-averaged propagation velocities of the diurnal variation between sites A and B (black circles) and sites B and C (cross marks) for the observation (solid lines) and model (dashed lines) during Period 2



in the year for most of September at site C (Fig. 6). On September 16, there was a meridional velocity signal from north to south; however, the diurnal variation was unclear (Fig. 7). Figure 8 shows the monthly mean propagation velocities between sites A and B and sites B and C. The period was from May to August 2013. September was excluded owing to unclear diurnal variations (Fig. 7). The propagation velocities between sites A and B increased gradually from $92 \text{ cm}\cdot\text{s}^{-1}$ in May to $164 \text{ cm}\cdot\text{s}^{-1}$ in August, whereas that between sites B and C was slower than that between sites A and B throughout the period, increasing from $65 \text{ cm}\cdot\text{s}^{-1}$ in May to $88 \text{ cm}\cdot\text{s}^{-1}$ in June.

The observation result analysis suggests that the diurnal variations are CTWs moving southward from the Tsugaru Strait along the Shimokita Peninsula. Their amplitudes have maxima in summer and late autumn and minima in spring and early autumn, and their propagation speed increases from spring to summer. In the following two sections, we analyze the model results to clarify the CTW structure and elucidate the causes of the characteristics indicated by the observations.

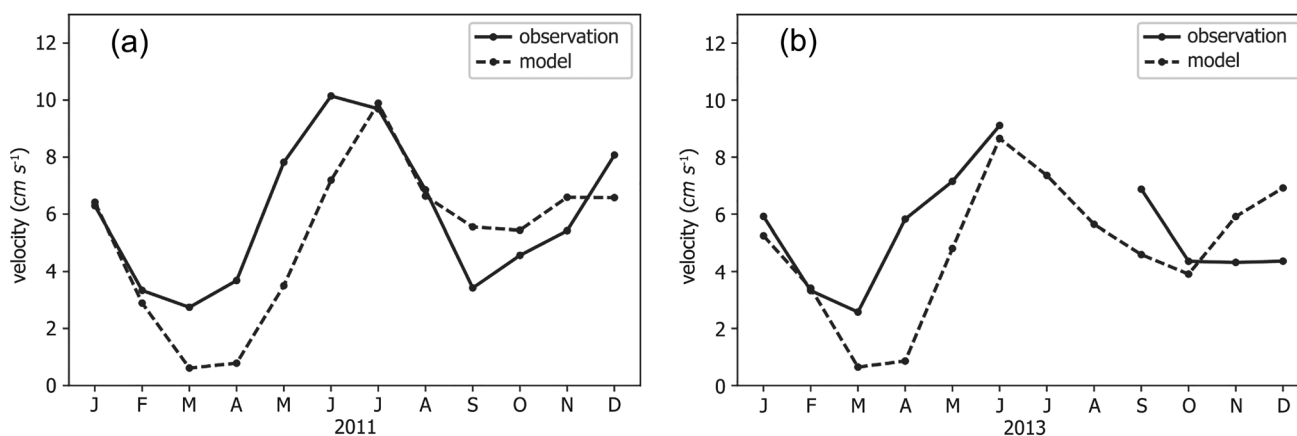


Fig. 9 Comparison of seasonal variation for the monthly-averaged magnitude of the CTWs in 2011 (a) and 2013 (b) between the observation (solid line) and model (dashed line)

6 Dependency of the CTWs on the stratification and shelf shape

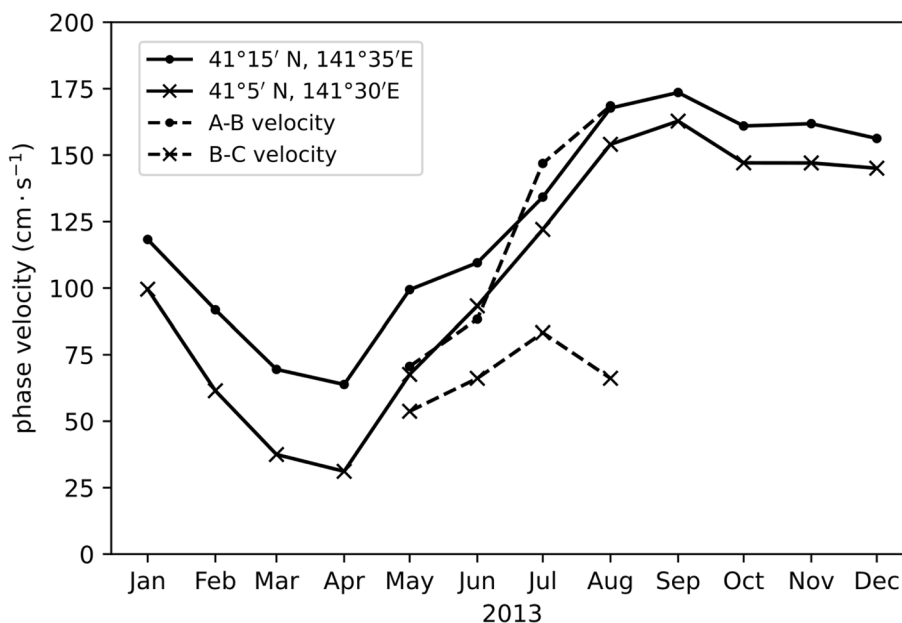
The model reproduces the CTWs with the same features as the observation. The propagation velocity of the CTWs of the model had the same trend from May to August 2013 as the observation (Fig. 8). Figure 9a, b show the monthly-averaged amplitude of the diurnal CTWs of the observation and the model in 2011 and 2013, respectively. Although both observed and modeled amplitudes show similar seasonal variations, the amplitude of the model is smaller from spring to early summer than that of the observation.

To compare the phase velocity of the reproduced CTWs and internal Kelvin waves, Fig. 10 shows a time series of the phase velocity for the first vertical-mode internal gravity wave from the model results. The representative values between sites A and B are shown at $41^{\circ}15' \text{ N}$ and $141^{\circ}35' \text{ E}$ and those between sites B and C at $41^{\circ}5' \text{ N}$ and $141^{\circ}30' \text{ E}$. For comparison, the propagation velocities of the variability between sites A and B and between sites B and C in the model are overlaid with dashed lines. The phase velocity at both sites decreased until April, then increased from May, peaked in September, and decreased gradually from October. The propagation velocity of the daily variability of the model between sites A and B was nearly consistent with the first mode of the model. The propagation speed between sites B and C differed from the phase speed of the internal gravity wave for the first mode and did not accelerate in summer. These results indicate that the CTWs behave as vertical first-mode internal Kelvin waves between sites A and B, whereas the shelf slope significantly influences those between sites B and C from July to August.

To examine the seasonal dependence of the Burger number, Fig. 11a, b shows the horizontal distribution of the first-mode internal deformation radius (λ_{D1}) using the monthly-averaged model values for April and October 2011, when the stratification was the weakest and strongest, respectively. The deformation radius was approximately 10 km in April 2011 and 18 km in October 2011 under the slope of the shelf at $41^{\circ}20' \text{ N}$ and $141^{\circ}40' \text{ E}$. South of approximately $41^{\circ}5' \text{ N}$, the isolines extend southeastward, corresponding to the eastward extension of the continental shelf. As shown in Fig. 1, the cross-shelf length L is about 10 km slightly north of $41^{\circ}5' \text{ N}$ of Shimokita Peninsula, and the slope is steep from the shelf to the deep sea. South of $41^{\circ}5' \text{ N}$, the shelf widens gradually to $L \sim 100 \text{ km}$ at $40^{\circ}40' \text{ N}$, and the shelf slope is gentler than that in the northern part. This indicates that the influence of shelf topography along the Shimokita Peninsula coast is more significant in the south than in the north.

We compared the structure of the CTWs in the northern and southern Shimokita Peninsula during the season of large internal deformation radius. Figures 12a–c illustrate the diurnal meridional velocity and potential density of the model on the zonal sections of $41^{\circ}15' \text{ N}$, 41° N , and $40^{\circ}40' \text{ N}$. The dates and times were 7:30 AM, 2:30 PM, and 7:30 PM on October 5, 2011, when the southward component of the diurnal velocity peaked during the day in the near-shore surface layer. At 7:30 AM and $40^{\circ}15' \text{ N}$ (Fig. 12a), the diurnal velocity up to approximately 15 km from the shore reversed at a depth of 200 m, which coincided with the node depth of the vertical first mode (the dashed line in Fig. 12a). The distance from the shore was comparable to the amplitude of the coastal Kelvin wave of the vertical first mode, which is the deformation radius for the mode during this period. This Kelvin wave-like structure indicates that

Fig. 10 Time series of the phase velocity of the first vertical-mode internal gravity wave (solid line) at $41^{\circ}15' \text{ N}$, $141^{\circ}35' \text{ E}$ and $41^{\circ}5' \text{ N}$, $141^{\circ}30' \text{ E}$, and the propagation velocities (dashed line) between sites A and B and sites B and C diagnosed with the model results



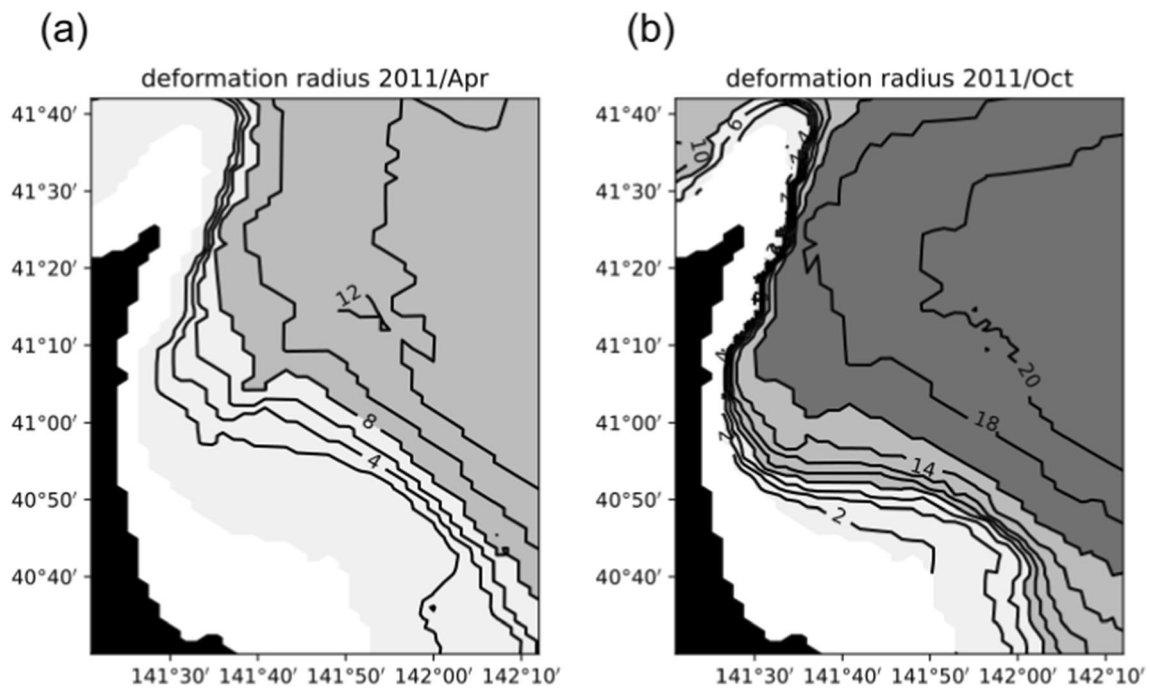


Fig. 11 Rossby internal deformation radius (km) for the first mode, diagnosed using the monthly average of the model. The time period is April 2011 (a) and October 2011 (b)

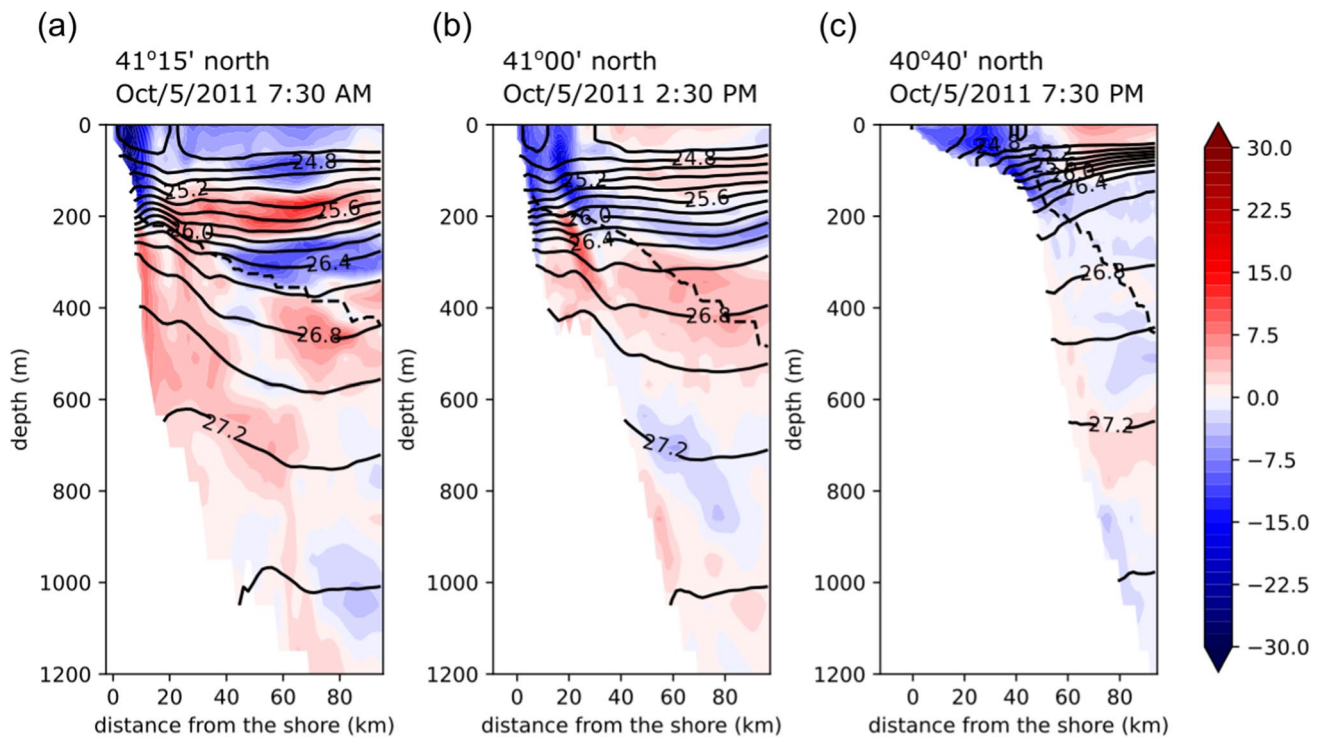


Fig. 12 Zonal vertical cross-sections of the diurnal meridional velocity (tones) and potential density (solid contours) at $41^{\circ}15'$ N (a), 41° N (b), and $40^{\circ}40'$ N (c). Dates and times are October 5, 2011, 7:30

AM (a), October 5, 2011, 2:30 PM (b), and October 5, 2011, 7:30 PM (c). Dashed lines represent the depth of the nodes in the first vertical mode

stratification had a stronger influence than the bottom slope. An S_1 value of approximately 3 in this vicinity, obtained with Eq. (3), supports this assumption. The density contours took a bowl shape, suggesting the presence of a TWC gyre. At 41° N (Fig. 12b), the diurnal velocities from the near-shore to a depth of 350 m were southward, whereas those from 350 m to the land shelf at 450 m were northward. Compared to $41^\circ 15'$ N (Fig. 12a), there was a southward flow at a lower level than the first modal node, which differs from the internal Kelvin wave structure. The velocities changed direction at a depth of 200 m at 20 km offshore from the coast, where the frontal structure of the western part of the gyre is located. These velocities were likely due to the variations in the front. As S_1 at this location was approximately 1, the slope contribution was significant compared with that of the $41^\circ 15'$ N section, which is comparable to the stratification contribution. At $40^\circ 40'$ N (Fig. 12c), a southward flow was observed over the shelf, and the shelf broke approximately 50 km from the shore. This structure differed significantly from the two northerly sections with vertical-mode structures. As the cross-shelf width here is significantly larger than that in the north, even when stratification was strong, S_1 was 0.02, which is small compared with 1. This result shows that the CTWs propagated southward in October, with a structural change from internal Kelvin waves to shelf waves.

However, uncertainty remains regarding the shelf waves in the southern part of the Shimokita Peninsula coastline because the transition process of CTWs in the cross-shelf width changing is complex (Wilkin and Chapman 1990). It is necessary to conduct velocity observations in the southern part of the Shimokita Peninsula coast to elucidate the transition process.

In spring, the shelf waters of the Shimokita Peninsula become weaker in density stratification due to the vertical uniformity of the TWC and the reduced density difference between the TWC and the Oyashio water. Figures 13a–c illustrate the diurnal meridional velocity and potential density of the model on the zonal sections of $41^\circ 15'$ N, $40^\circ 5'$ N, and 40° N. The dates and times were 6:30 PM on April 5, 2011, and 5:30 AM and 7:30 PM on April 6, 2011. During this period, the stratification was the weakest for the year. At $41^\circ 15'$ N (Fig. 13a), the upper layer had a nearly vertical uniform flow until approximately 400 m below the surface, extending 10 km from the shore. In contrast, the lower layer was trapped on the slope at approximately 400–650 m depth. It extended further offshore than the upper layer due to an S_1 value of approximately 0.5, which slightly differs from the structure of the internal Kelvin waves. At $41^\circ 5'$ N (Fig. 13b), the current velocities were smaller, with several kilometers of southward flow in the upper 200 m depths

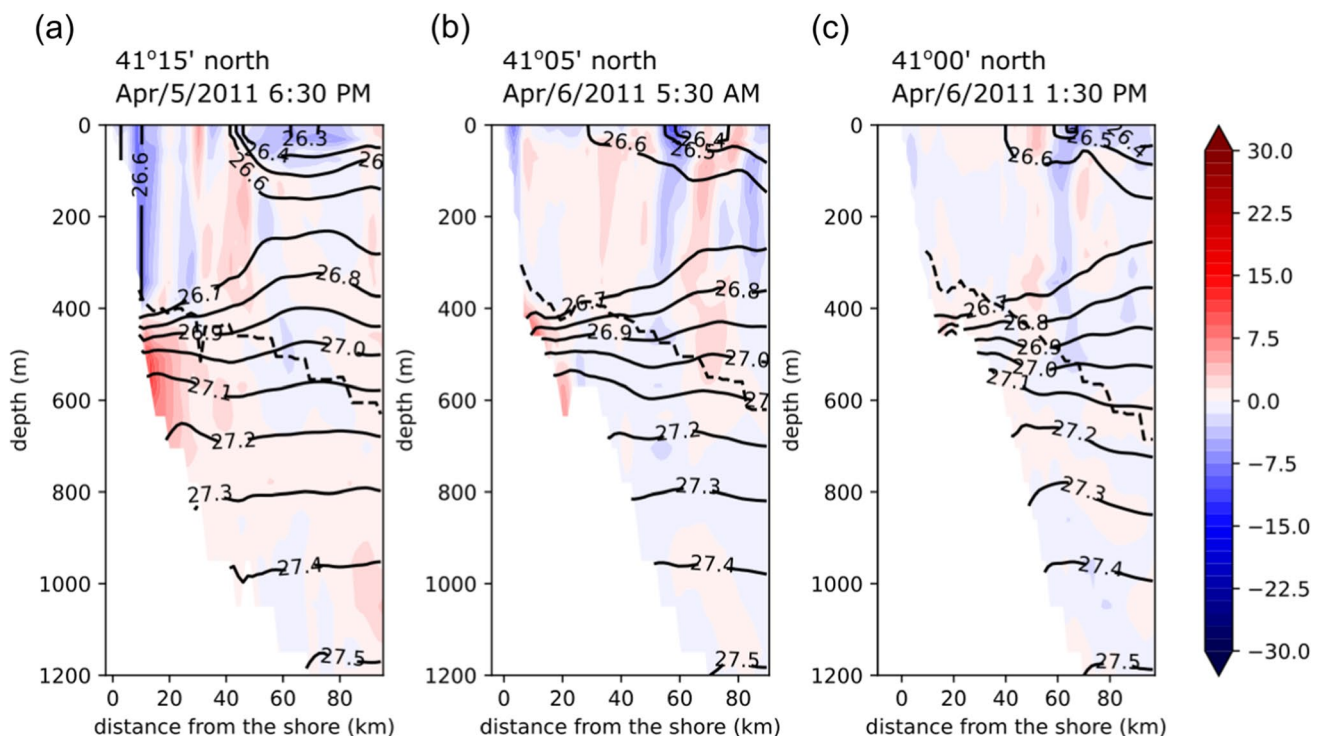


Fig. 13 Zonal vertical cross-sections of the diurnal meridional velocity (tones) and potential density (solid contours) at $41^\circ 15'$ N (a), $41^\circ 5'$ N (b), and 41° N (c). Dashed lines represent the depth of the nodes

in the first vertical mode. Dates and times are 6:30 PM on April 5, 2011 (a), and 5:30 AM (b) and 1:30 PM on April 6, 2011 (c)

and countercurrents trapped on the seafloor at depths of 400–650 m. At this latitude, as S_1 was approximately 0.2, the stratification contribution was significantly smaller than that at 41°15' N. This structure is similar to that in the weak stratification experiment of Huthnance (1978), indicating a typical CTW structure in weak stratification. The mean propagation velocity from 41°15' N was $25 \text{ cm}\cdot\text{s}^{-1}$, which is comparable to the phase velocity of the first-mode internal gravity wave. Further south, the daily periodic variation in the coastal current velocity had almost no wave propagation until 41° N (Fig. 13c)

These results are consistent with the climatological values of the observations at site C in Fig. 6, with minima in March and April. The stratification was weak in this season, and the density was almost constant in the vertical direction to a depth of 300 m near the coast at 41°5' N. The contributions of gravity due to the weak stratification and topographic beta with the small cross-section width of the shelf were small; thus, the CTWs hardly propagated along the Shimokita coast in spring.

7 Influence of seasonal variations in the TWC flow route on the Tsugaru Strait

Although, in September, the strong stratification in this area suggests that the CTW strength should be comparable to that in the summer and early winter, it was minimal (Fig. 9a), indicating that the weakening in September was due to causes different from those in spring. In this section, we focus on the seasonal variation in the TWC axis in the CTW generation area, exploring the causes of this weakening.

The diurnal velocity magnitude was the largest in July (Fig. 6). Figure 14a–d show the horizontal distribution of diurnal horizontal velocities at 32 m depth and diurnal vertical velocities at 109 m depth. Figure 15a–d show the vertical cross-sections of the lines in Fig. 14a–d, respectively. At 5:30 AM, the horizontal diurnal current in the Tsugaru Strait flowed from approximately 41°40' N and 141°20' E toward the east and southeast and expanded on the sill adjacent to Cape Shiriya (Fig. 14a). Strong currents near Cape Shiriya and the northern tip of the sill produced downward vertical currents downstream of each other. These two fast downward flows were located around the south-southwestward flows, as seen at approximately 41°28' N and 41°38' N (Figs. 14a and 15a). The current was weak along the eastern coast of the Shimokita Peninsula, south of 41°20' N (Fig. 15a). From 8:30 to 11:30 AM, the horizontal velocities over the sill weakened (Fig. 14b, c). A south-southwestward flow occurred below the shelf slope at approximately 41°N, and this flow had a vertical first-mode structure (Figs. 15b, c). The horizontal distribution of the vertical flow extended

southwest along the shelf slope, east of the sill (Fig. 14b, c). These features correspond to first-mode Kelvin waves. At 2:30 PM, the flow near the sill turned toward the northwest (Fig. 14d), and the southward flow due to the CTW shifted to the south at approximately 41°25' N (Fig. 15d). The vertical profile of the density surface displayed in Fig. 15a–d shows that the $25.75 \sigma_\theta$ line at 41°30' N was approximately 150 m at 5:30 AM (Fig. 15a), and the large downward velocity depressed the surface to approximately 200 m at 11:30 AM (Fig. 15c). During the same period, the $26 \sigma_\theta$ isopycnal line was depressed by approximately 20 m from 200 m (Fig. 15a, c). The propagation of this wave followed a south-southwest direction on this isopycnal surface. For instance, the $26 \sigma_\theta$ lines at 41°10' N were depressed by approximately 60 m at 2:30 PM compared to that at 5:30 AM (Fig. 15a, d). This feature indicates that the CTW occurred between 41°25' N and 41°30' N. The flow near Cape Shiriya and over the sill formed a downwelling current that lowered the isopycnal surface, generating waves. The upward vertical flow velocity near 41°35' N at 5:30 AM was not directed south-southwest along the shelf but propagated eastward (Fig. 14a–d).

To investigate the cause of the weakening of the diurnal variation in autumn, we compared September with July, when it was at its maximum. Figures 16a–d and 17a–d show the same results as those in Figs. 14a–d and 15a–d, respectively, but for every 3 h from 2:30 PM on September 18, 2011. In July, a significant diurnal flow was present on the sill near Cape Shiriya (Fig. 14a–d), but in September (Fig. 16a–d), the flow on the sill was weaker than in July. The flow was strong near the cape in July (Fig. 14a, b), whereas in September, the diurnal flow was present only near the northeastern end of the sill (around 41°40' N, 141°30'–35' E), and it was weak near the cape (Fig. 16b, c). Corresponding to the horizontal velocity distribution, the diurnal vertical flow east of the sill was limited to the vicinity of 41°35'–40' N, 141°30' E (Fig. 16b, c). The southwesterly flow and vertical direct current along the land shelf of Shimokita Peninsula (Fig. 14a–d), as seen in July, were virtually non-existent (Fig. 16a–d). This was confirmed by the vertical profile (Fig. 17a–d), which shows that south of 41°20' N, the southwesterly flow at the surface was a few $\text{cm}\cdot\text{s}^{-1}$. The vertical first-mode structure, as seen in July, was indistinct. The diurnal variations in the strait hardly contributed to the excitation of the CTWs, which propagated eastward along the TWC at approximately 41°40' N, as shown in the horizontal distribution in Fig. 16a–d. The CTW was strong in July and weak in September, depending on whether the tidal current passed over the sill slope between 41°25' N and 41°30' N, where the CTW arises. As shown by the daily mean velocities for each day, the TWC flowed across the sill on July 28 (Fig. 18a), whereas it flowed east-northeastward

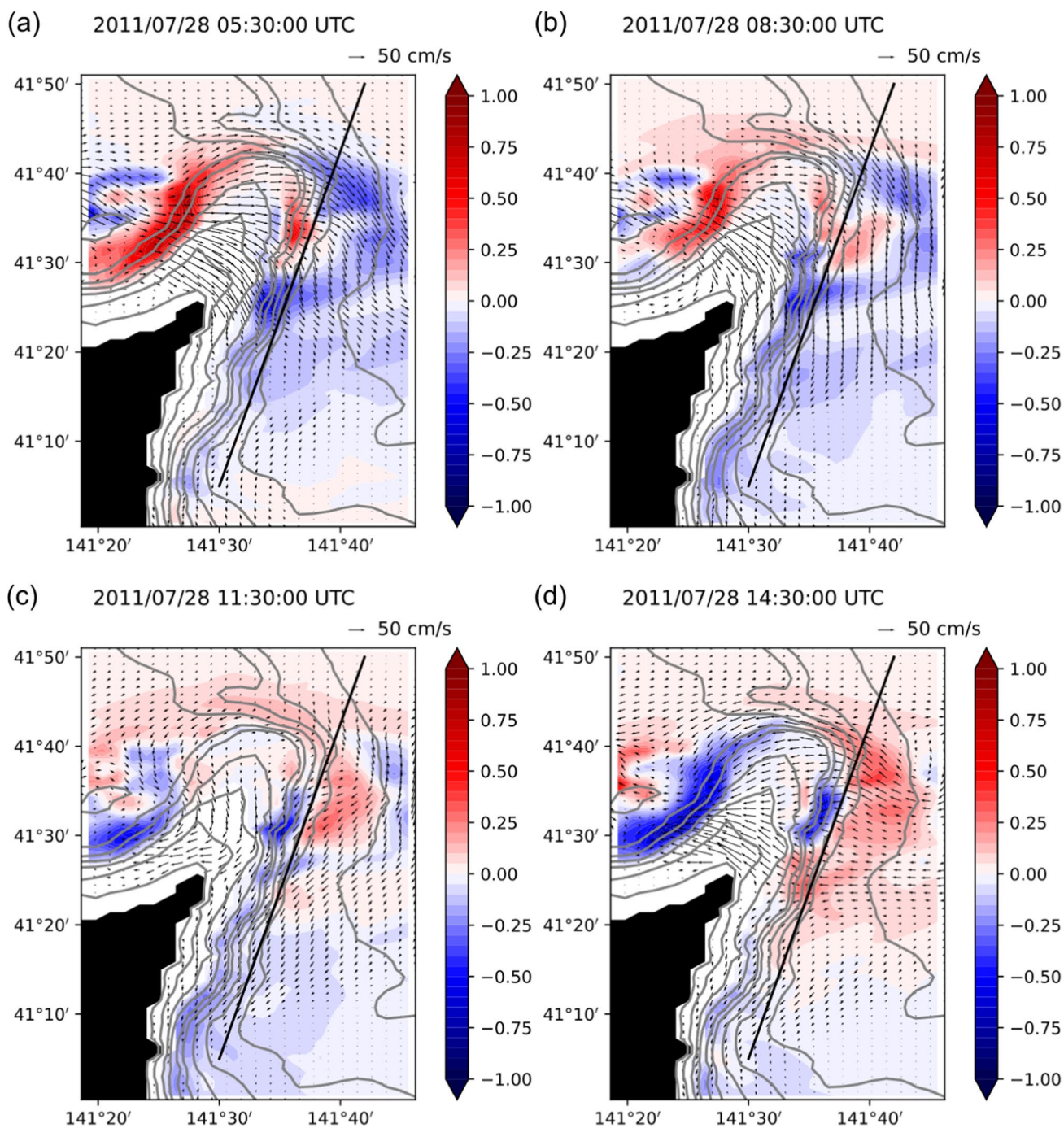


Fig. 14 Horizontal distribution of diurnal horizontal velocities (vectors) at 32 m depth and vertical velocities (tones) at 109 m depth. Gray contours represent seafloor depths of 25, 50, 75, 100, 150, 200, 300, 400, 500, 750, and 1000 m, respectively. Solid lines represent

the sections in Fig. 15. The dates and times are 5:30 AM on July 28, 2011 (a), 8:30 AM on the same day (b), 11:30 AM on the same day (c), and 2:30 PM on the same day (d)

over the northeasternmost portion of the sill on September 18 (Fig. 18b).

Figure 19 shows the seasonal shift in the TWC axis during 2011. The latitude of the maximum velocity at

141°10' E in the Tsugaru Strait defines the TWC axis. The latitude of the TWC was to the south until July, moved north in August, reached its northernmost extent in the first half of September, and then moved south from

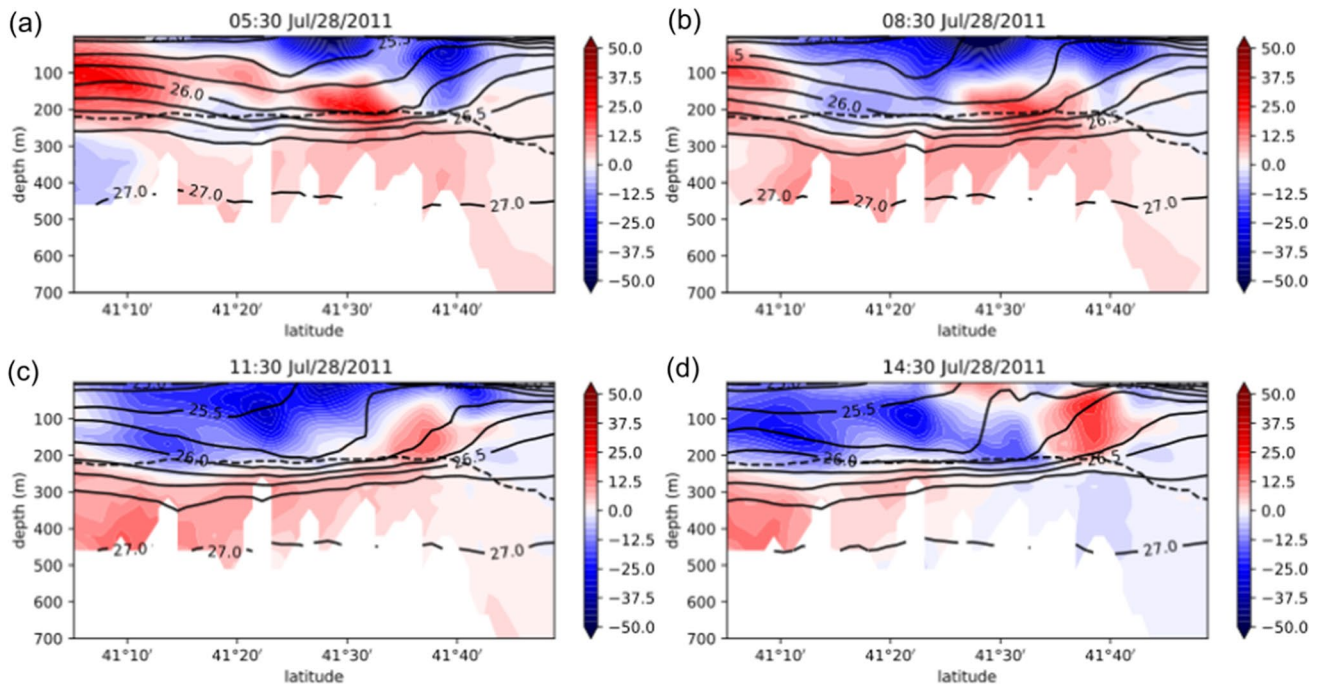


Fig. 15 Vertical cross-sections of the black lines in Fig. 14 show diurnal velocity (tone; northeastward is positive) and potential density (solid contours). Dashed lines represent the depth of the nodes in the

first vertical mode. The dates and times are 5:30 AM on July 28, 2011 (a), 8:30 AM on the same day (b), 11:30 AM on the same day (c), and 2:30 PM on the same day (d)

November to December. Observations have indicated this seasonal change in the position of the TWC in the eastern part of the Tsugaru Strait. Yasui et al. (2022) reported that the HF radar within the Tsugaru Strait from 2014 to 2020 showed that the axis of the TWC is southerly in April near Cape Shiria and moves northward until September, which then turns southward from October onward. These results indicate that the CTW weakened in autumn because the interference between the TWC and sill decreased owing to the northward shift of the TWC axis in the Tsugaru Strait.

8 Discussion

Continuous velocity observations at site C indicated that semi-daily fluctuations are weak on the Pacific side of the Shimokita Peninsula. Observations within the Tsugaru Strait showed that the amplitudes of semidiurnal currents are large, and M2 is comparable in magnitude to K1 and O1 (Onishi et al. 2004). The reason for this difference is that at 41°N (latitude of the target area), the semidiurnal tide is super-inertial; thus, free-traveling waves propagate without being trapped by the coast.

In the model, barotropic tidal waves in the Tsugaru Strait came in contact with the sill at Cape Shiria and changed into CTWs, but several waves propagated eastward along the TWC. Particularly in autumn, when the axis of the TWC shifts to the north, the waves propagate eastward with little interference from the Cape Shiria sill. Although it is unclear whether such a phenomenon exists, satellite and HF radar observations can be used for clarification in the future.

Wang and Mooers (1976) formulated eigenmodes based on stratification and continental shelf slope. In the northern part of the coast of the Shimokita Peninsula, the cross-shelf width is small, and the slope is steep, so ignoring the effect of slope inclination does not make a significant difference. Neglecting the bottom slope term in their Eq. (29a) is identical to the vertical mode. On the south side, the land shelf is wider toward the south, and this Equation is no longer applied in case the shelf width varies. Webster (1987) and Wilkin and Chapman (1990) have studied the behavior of CTWs when continental shelf width changes. The transition process of CTWs with shelf width changes in the target area is not fully clarified in this paper, warranting future work.

The model had several inconsistencies with the observations. The position of the Tsugaru Gyre occasionally differed from that estimated from XCTD observations on the ferry

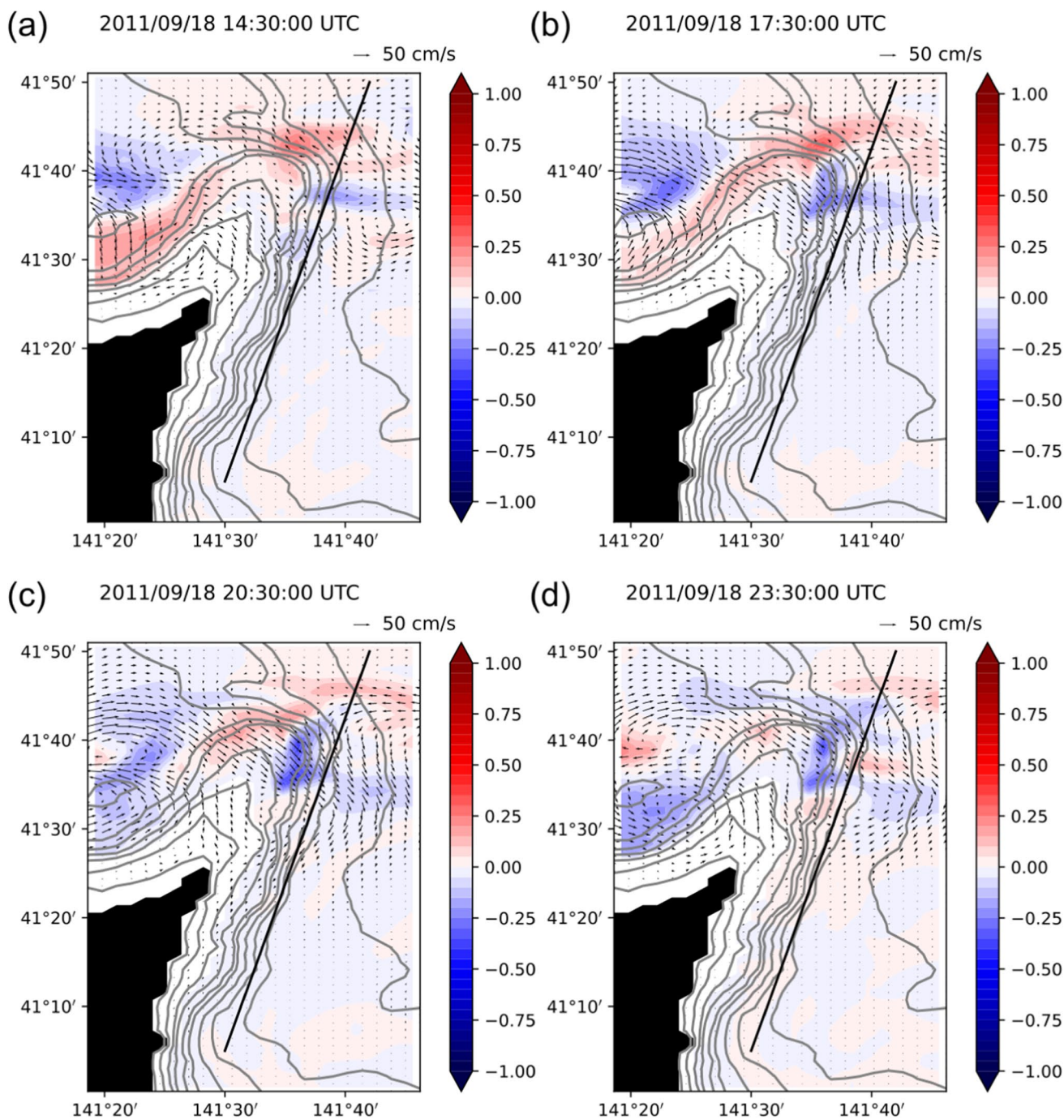


Fig. 16 Horizontal distribution of diurnal horizontal velocities (vectors) at 32 m depth and vertical velocities (tones) at 109 m depth. Gray contours represent seafloor depths of 25, 50, 75, 100, 150, 200,

300, 400, 500, 750, and 1000 m. Solid lines represent the sections in Fig. 17. The date is September 18, 2011, and the times are 2:30 PM (a), 5:30 PM (b), 8:30 PM (c), and 11:30 PM (d)

route. Because the north–south position of the Tsugaru Gyre could correspond to the TWC near Cape Shiriya, the southward position of the modeled Tsugaru Gyre suggests that the axis of the TWC near Cape Shiriya may also be located more

to the south than that in reality. This southward bias of the TWC explains why the magnitude of the modeled autumn diurnal cycle was larger than that observed. Another issue is that the diurnal variability of the model in spring was

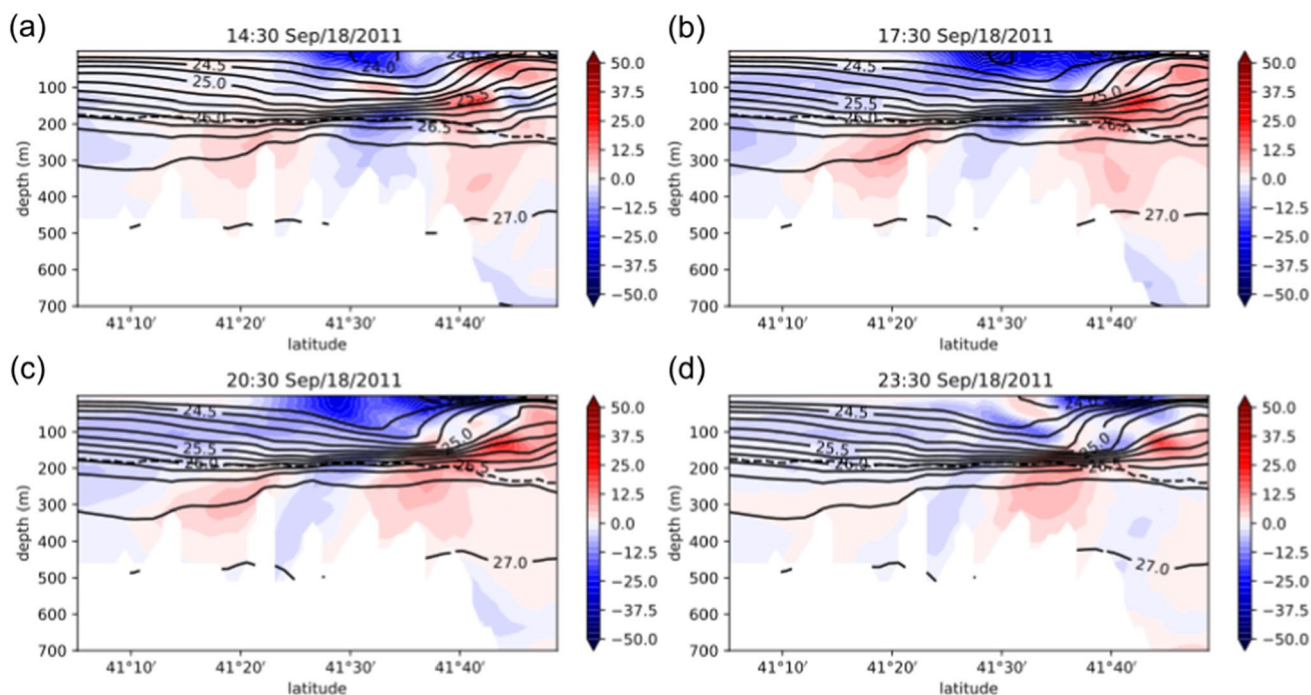
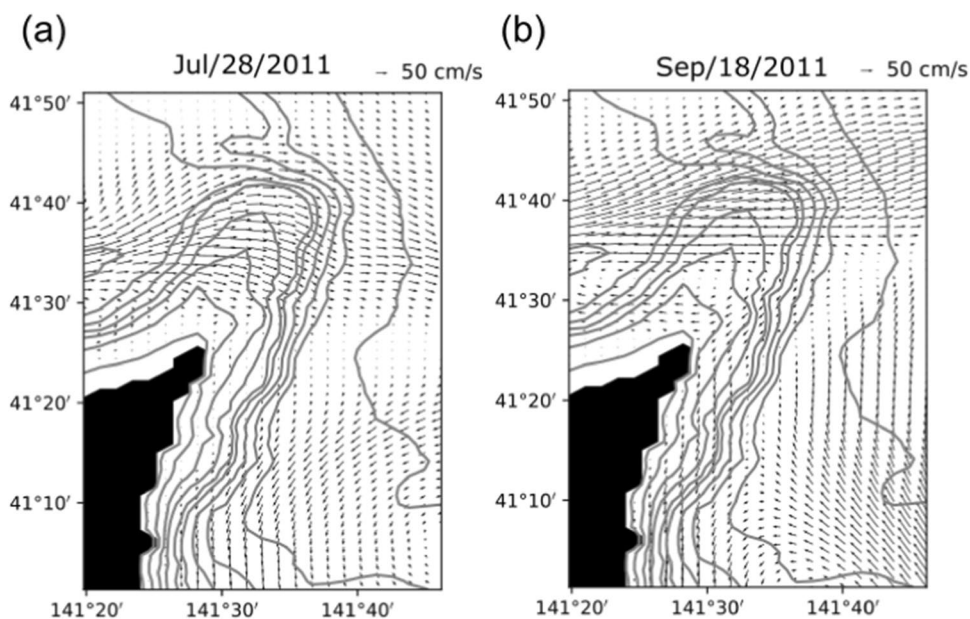


Fig. 17 Vertical cross-sections of the black lines in Fig. 16 show diurnal velocity (tone; northeastward is positive) and potential density (solid contours). Dashed lines represent the depth of the node in the

first vertical mode. The date is September 18, 2011, and the times are 2:30 PM (a), 5:30 PM (b), 8:30 PM (c), and 11:30 PM (d)

Fig. 18 Horizontal distribution of daily mean horizontal velocity at 32 m depth. Gray contours represent seafloor depths of 25, 50, 75, 100, 150, 200, 300, 400, 500, 750, and 1000 m. Dates are July 28, 2011 (a) and September 18, 2011 (b)

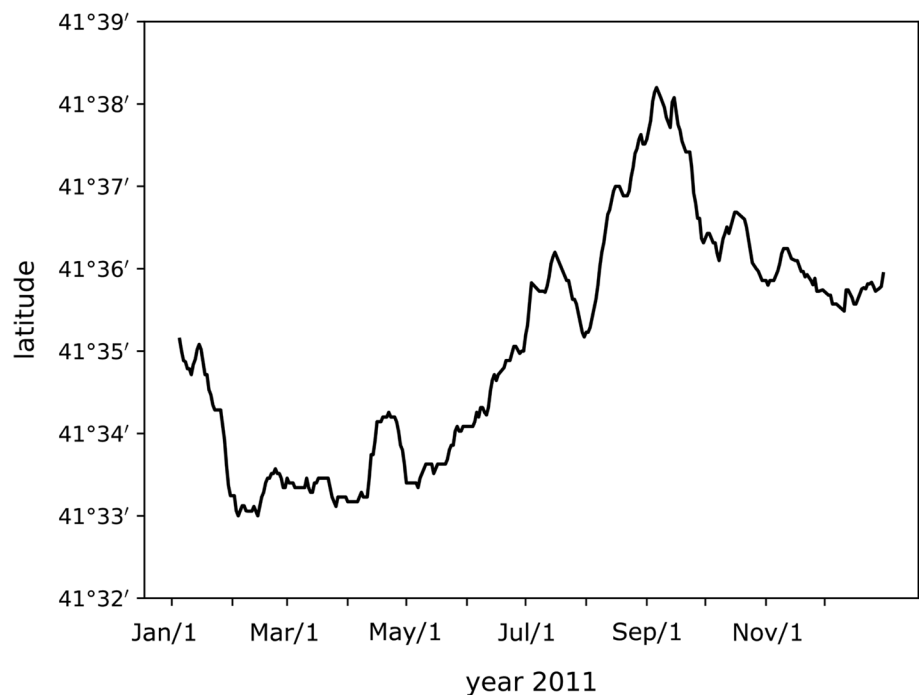


smaller than that observed. This bias may be because the land shelf on the northern side of the Shimokita Peninsula is narrow, and the model resolution does not adequately reproduce the flow over such a narrow shelf.

9 Conclusion and future work

We studied the diurnal CTWs in the coastal region of the Shimokita Peninsula using continuous current observations and an ocean model. These waves originate from the sill of Cape Shiriya and propagate southward. From

Fig. 19 Seasonal variation of the flow axis latitude of the TWC within the Tsugaru Strait at 141°10'N in 2011



summer to early winter, the CTWs propagated north of 41°N as baroclinic coastal Kelvin waves in the first vertical mode whereas they propagated south of 41°N as land shelf waves because the shelf is broader than that at the northern part. CTWs tended to weaken in autumn because the TWC moves northward near Cape Shiriya, weakening the interference with sills that connect to the cape. From late winter to spring, the CTWs ceased to propagate in the northern part of the Shimokita Peninsula because of the narrower cross-shelf width in this area and the weak stratification during this period. This study helps clarify short-term variations in the coastal area of the Shimokita Peninsula and the prediction of mass transport and fisheries in this area.

In this study, we have not been able to fully elucidate the migration process of the CTWs due to the change in the cross-shelf width from the northern to the southern part of the Shimokita Peninsula coast, so we will use observations and modeling approaches to elucidate this process in future studies.

The model in this study reproduced the waves generated at the sill near Cape Shiria that moved southward along the

coast of the Shimokita Peninsula as CTWs, whereas they moved eastward along the TWC. The eastward waves propagate both with diurnal and semidiurnal periods. We will clarify their features and characteristics to reveal the short-term variations east of the Shimokita Peninsula.

Appendix A

Figures 20, 21, 22 and 23 show the vertical distribution of XCTD observations and model values along the ferry route (Fig. 2b) during Periods 1 and 2 of the velocity observation at sites A and B in Fig. 2a. During Period 1 (Figs. 20 and 21), the observations and model showed temperatures above 6 °C and water salinity above 33.7, which was classified as the TWC (a bowl-shaped water mass reaching a depth of approximately 300 m) Hanawa and Mitsudera (1986). This structure suggests the existence of a clockwise circulation based on the thermal-wind relation. During Period 2 (Figs. 22 and 23), the gyre was in the process of growing.

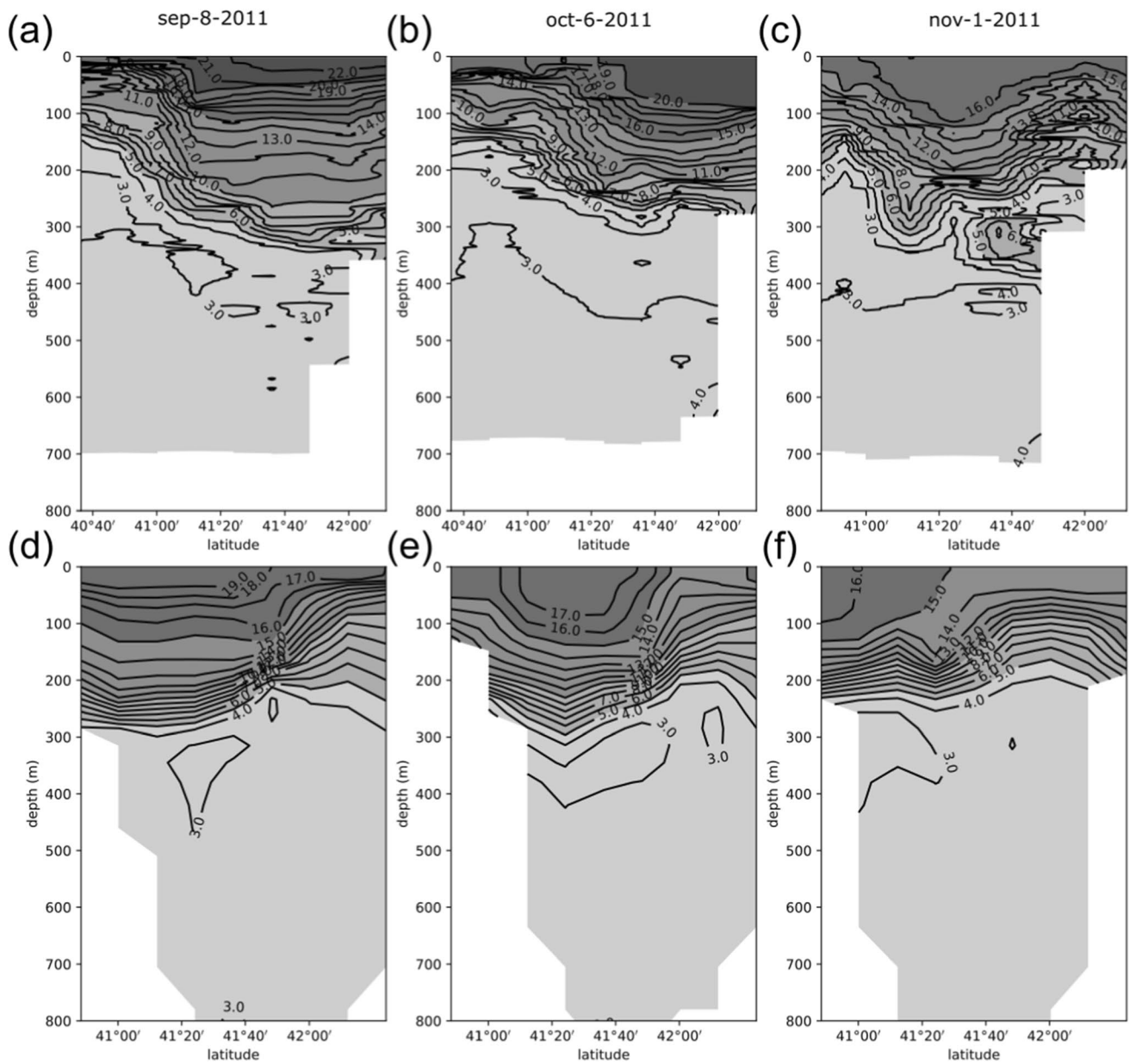


Fig. 20 Vertical temperature profiles for XCTD observations on the ferry ship route (a-c) and the model on the same route (d-f). Dates from left to right: September 8 (a, d), October 6 (b, e), and November 1 (c, f), 2011

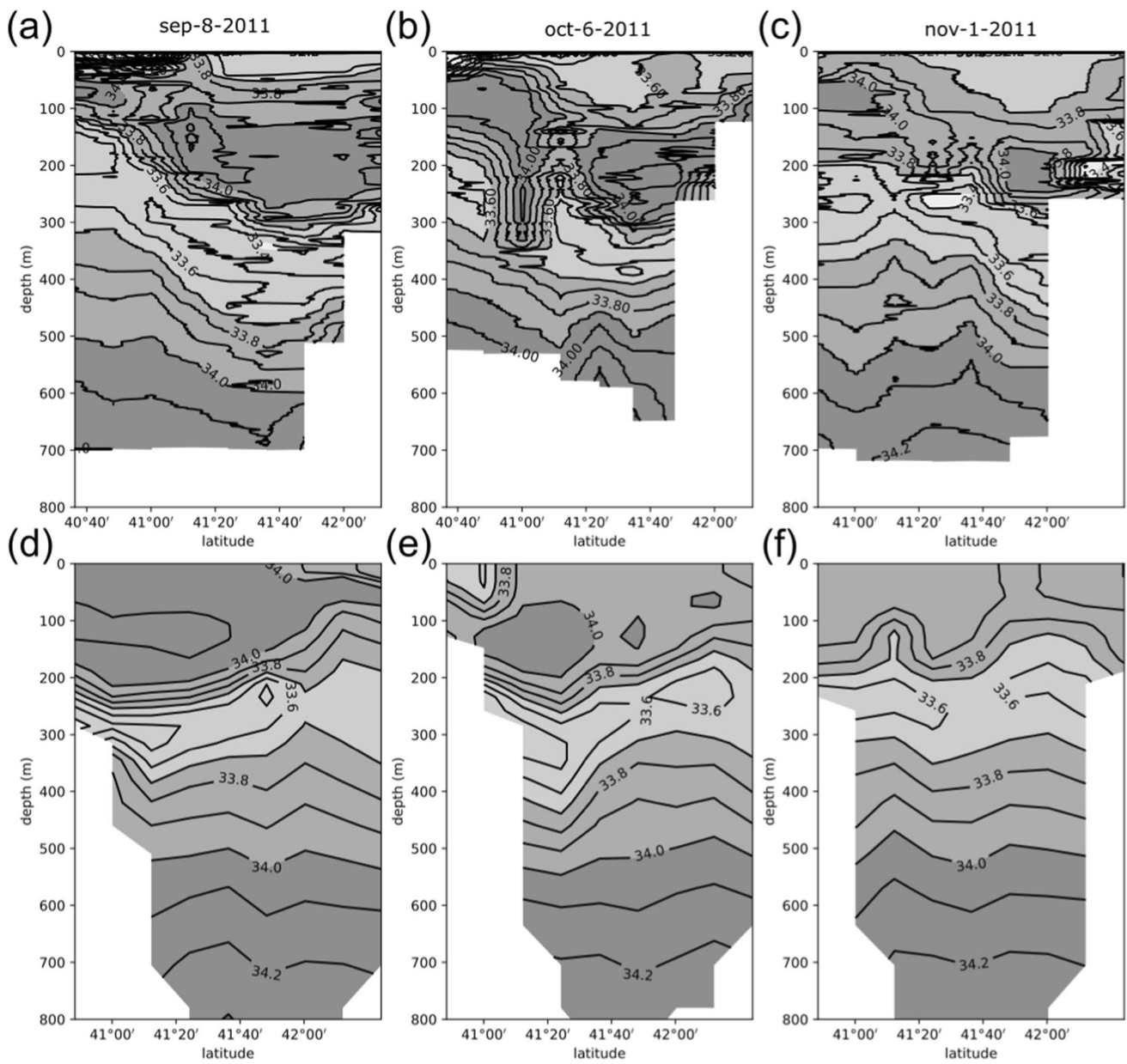


Fig. 21 Vertical salinity profiles for XCTD observations on the ferry ship route (a-c) and the model on the same route (d-f). Dates from left to right: September 8 (a, d), October 6 (b, e), and November 1 (c, f), 2011

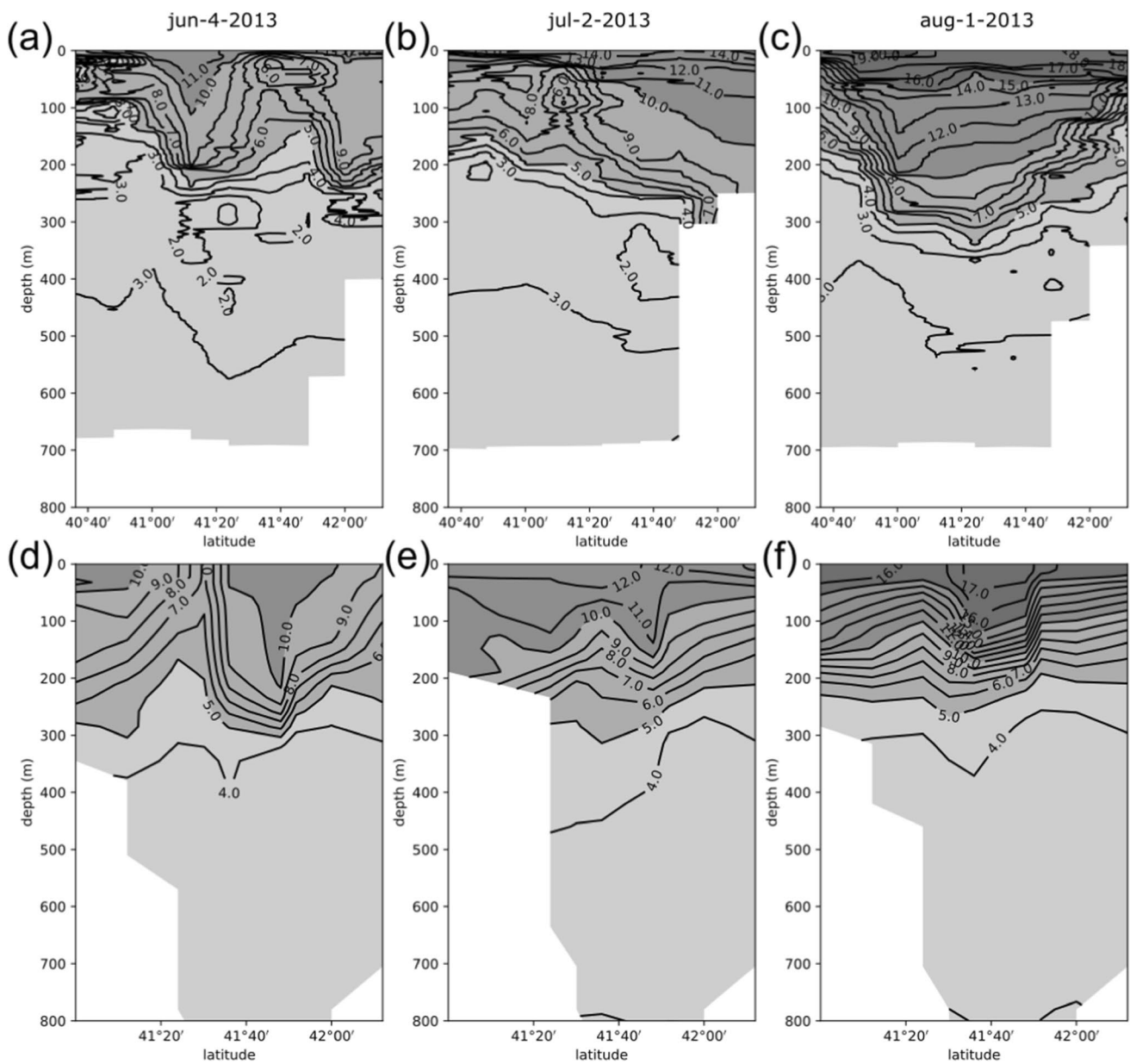


Fig. 22 Vertical temperature profiles for XCTD observations on the ferry ship route (a-c) and the model on the same route (d-f). Dates from left to right: June 4 (a, d), July 2 (b, e), and August 1 (c, f), 2013

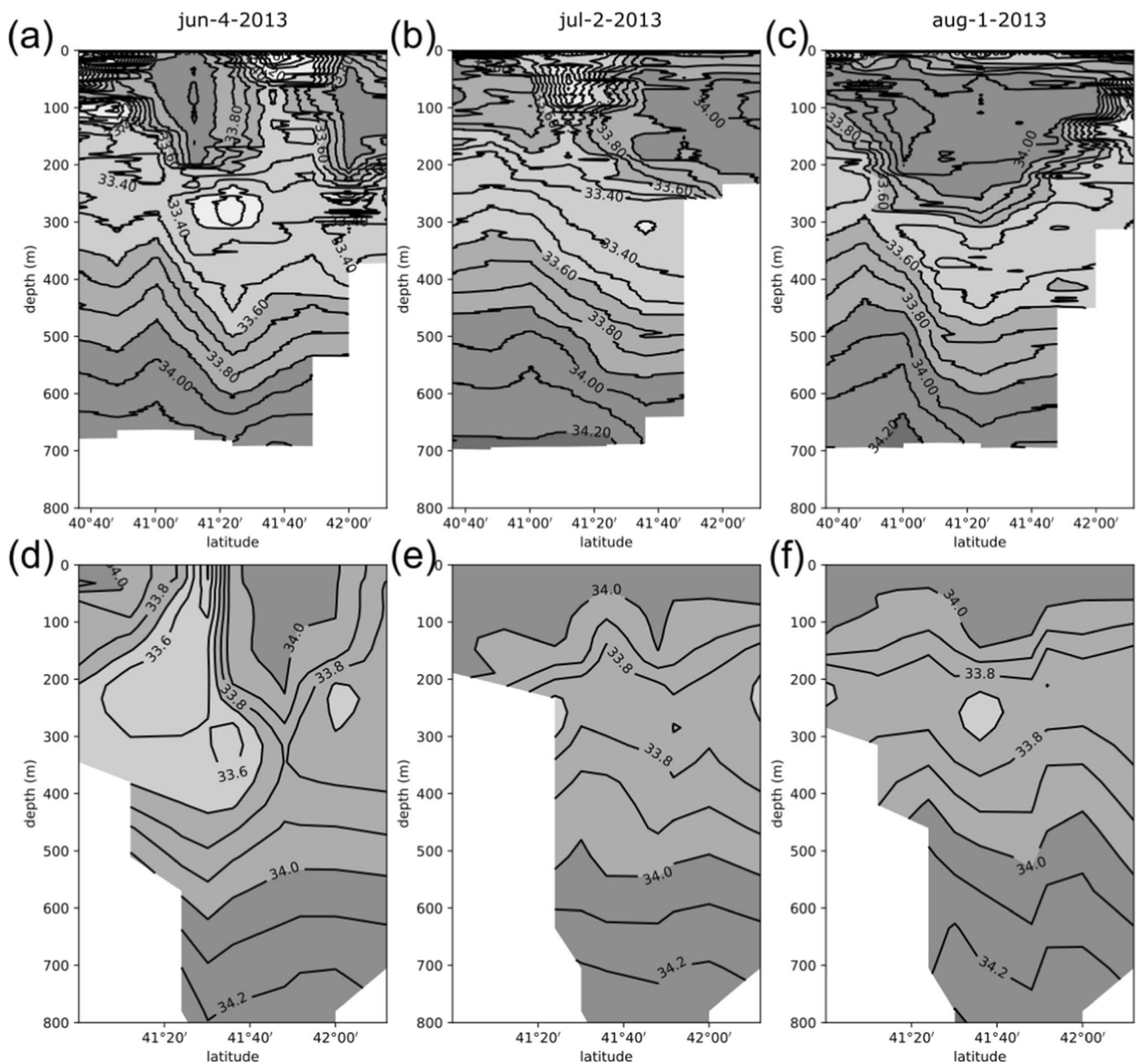


Fig. 23 Vertical salinity profiles for XCTD observations on the ferry ship route (a–c) and the model on the same route (d–f). Dates from left to right: June 4 (a, d), July 2 (b, e), and August 1 (c, f), 2013

Acknowledgements A part of this research was conducted under contract with Aomori Prefecture. This study utilized the dataset ‘Four-dimensional Variational Ocean Reanalysis for the Western North Pacific’ (FORA-WNP30), which was produced by the Japan Agency for Marine-Science and Technology (JAMSTEC) and Meteorological Research Institute of Japan Meteorological Agency (JMA/MRI).

Data availability The data in this paper are available with permission from the Japan Marine Science Foundation and Aomori Prefecture.

Open Access This article is licensed under a Creative Commons Attribution 4.0 International License, which permits use, sharing, adaptation, distribution and reproduction in any medium or format, as long as you give appropriate credit to the original author(s) and the source,

provide a link to the Creative Commons licence, and indicate if changes were made. The images or other third party material in this article are included in the article’s Creative Commons licence, unless indicated otherwise in a credit line to the material. If material is not included in the article’s Creative Commons licence and your intended use is not permitted by statutory regulation or exceeds the permitted use, you will need to obtain permission directly from the copyright holder. To view a copy of this licence, visit <http://creativecommons.org/licenses/by/4.0/>.

References

- Brink KH (1982) A comparison of long coastal trapped wave theory with observations off Peru. *J Phys Oceanogr* 12:897–913. [https://doi.org/10.1175/1520-0485\(1982\)012%3c0897:ACOLCT%3e2.0.CO;2](https://doi.org/10.1175/1520-0485(1982)012%3c0897:ACOLCT%3e2.0.CO;2)
- Conlon DM (1982) On the outflow modes of the Tsugaru Warm Current. *La Mer* 20:60–64
- Gent PR, McWilliams JC (1990) Isopycnal mixing in ocean circulation models. *J Phys Oceanogr* 20:150–155. [https://doi.org/10.1175/1520-0485\(1990\)020%3c0150:IMIOC%3e2.0.CO;2](https://doi.org/10.1175/1520-0485(1990)020%3c0150:IMIOC%3e2.0.CO;2)
- Gill AE (1982) Atmosphere-ocean dynamics, vol. 30 of International Geophysics Series. Academic Press, San Diego, p 666
- Griffies S, Hallberg RW (2000) Biharmonic friction with a Smagorinsky-like viscosity for use in large-scale eddy-permission ocean models. *Mon Weather Rev* 128:2935–2946. [https://doi.org/10.1175/1520-0493\(2000\)128%3c2935:BFWASL%3e2.0.CO;2](https://doi.org/10.1175/1520-0493(2000)128%3c2935:BFWASL%3e2.0.CO;2)
- Hanawa K, Mitsudera H (1986) Variation of water system distribution in the Sanriku coastal area. *J Oceanogr* 42:435–446
- Hatayama T, Awaji T, Akitomo K (1996) Tidal currents in the Indonesian Seas and their effect on transport and mixing. *J Geophys Res Oceans* 101:12353–12373. <https://doi.org/10.1029/96JC00036>
- Homma S, Saruwatari A, Miyatake M (2017) Characterization of the three dimensional density structure in the Tsugaru Strait. *J JSCIE* 73:67–72 (in Japanese with English abstract)
- Huthnance JM (1978) On coastal trapped waves: analysis and numerical calculation by inverse iteration. *J Phys Oceanogr* 8:74–92. [https://doi.org/10.1175/1520-0485\(1978\)008%3c0074:OCT-WAA%3e2.0.CO;2](https://doi.org/10.1175/1520-0485(1978)008%3c0074:OCT-WAA%3e2.0.CO;2)
- Isobe A (1999) On the origin of the Tsushima Warm Current and its seasonality. *Cont Shelf Res* 19:117–133. [https://doi.org/10.1016/S0278-4343\(98\)00065-X](https://doi.org/10.1016/S0278-4343(98)00065-X)
- Ito T, Togawa O, Ohnishi M et al (2003) Variation of velocity and volume transport of the Tsugaru Warm Current in the winter of 1999–2000. *Geophys Res Lett.* <https://doi.org/10.1029/2003GL017522>
- Kanamitsu M, Ebisuzaki W, Woollen J et al (2002) NCEP-DOE AMIP II reanalysis (R-2). *Bull Am Meteorol Soc* 83:1631–1643. <https://doi.org/10.1175/BAMS-83-11-1631>
- Kuroda H, Isoda Y, Ohnishi M, Iwahashi et al (2004) Examination of harmonic analysis methods using semi-regular sampling data from an ADCP installed on a regular ferry: evaluation of tidal and residual currents in the Eastern Mouth of the Tsugaru Strait. *Oceanogr Japan* 13:553–564. <https://doi.org/10.5928/kaiyou.13.553>
- Luu Q-H, Ito K, Ishikawa Y, Awaji T (2011) Tidal transport through the Tsugaru Str—it—part I: characteristics of the major tidal flow and its residual current. *Ocean Sci J* 46:273–288. <https://doi.org/10.1007/s12601-011-0021-z>
- Matsumoto K, Takanezawa T, Ooe M (2000) Ocean tide models developed by assimilating TOPEX/POSEIDON altimeter data into hydrodynamical model: a global model and a regional model around Japan. *J Oceanogr* 56:567–581. <https://doi.org/10.1023/A:1011157212596>
- Noh Y, Kim HJ (1999) Simulations of temperature and turbulence structure of the oceanic boundary layer with the improved near-surface process. *J Geophys Res Oceans* 104:15621–15634. <https://doi.org/10.1029/1999jc900068>
- Odamaki M (1994) Tides and tidal currents along the Okhotsk coast of Hokkaido. *J Oceanogr* 50:265–279. <https://doi.org/10.1007/BF02239517>
- Onishi M, Ohtani K (1997) Volume transport of the Tsushima Warm Current, west of Tsugaru Strait bifurcation area. *J Oceanogr* 53:27–34. <https://doi.org/10.1007/BF02700746>
- Onishi M, Isoda Y, Kuroda H et al (2004) Winter transport and tidal current in the Tsugaru Strait. *Bull Fish Sci Hokkaido Univ* 55:105–119
- Saito K, Fujita T, Yamada Y et al (2006) The operational JMA non-hydrostatic mesoscale model. *Mon Weather Rev.* <https://doi.org/10.1175/MWR3120.1>
- Shikama N (1994) (in Japanese) Current measurements in the Tsugaru Strait using bottom-mounted ADCPs. *KAIYO Monthly* 26:815–818
- Usui N, Wakamatsu T, Tanaka Y et al (2017) Four-dimensional variational ocean reanalysis: a 30-year high-resolution dataset in the western North Pacific (FORA-WNP30). *J Oceanogr* 73:205–233. <https://doi.org/10.1007/s10872-016-0398-5>
- Wang D-P, Mooers CNK (1976) Coastal-trapped waves in a continuously stratified ocean. *J Phys Oceanogr* 6:853–863. [https://doi.org/10.1175/1520-0485\(1976\)006%3c0853:CTWIAC%3e2.0.CO;2](https://doi.org/10.1175/1520-0485(1976)006%3c0853:CTWIAC%3e2.0.CO;2)
- Webster I (1987) Scattering of coastal trapped waves by changes in continental shelf width. *J Phys Oceanogr* 17:928–937. [https://doi.org/10.1175/1520-0485\(1987\)017%3c0928:SOCTWB%3e2.0.CO;2](https://doi.org/10.1175/1520-0485(1987)017%3c0928:SOCTWB%3e2.0.CO;2)
- Wilkin JL, Chapman DC (1990) Scattering of coastal-trapped waves by irregularities in coastline and topography. *J Phys Oceanogr* 20:396–421. [https://doi.org/10.1175/1520-0485\(1990\)020%3c0396:SOCTWB%3e2.0.CO;2](https://doi.org/10.1175/1520-0485(1990)020%3c0396:SOCTWB%3e2.0.CO;2)
- Yasui T, Abe H, Hirawake T, Sasaki K, Wakita M (2022) Seasonal pathways of the Tsugaru warm Current revealed by high-frequency ocean radars. *J Oceanogr* 78:103–119. <https://doi.org/10.1007/s10872-022-00631-y>